



Probing Dark Energy and Modifications of Gravity with Ground-based millimeter-wavelength Line Intensity Mapping

Azadeh Moradinezhad Dizgah¹ , Emilio Bellini^{2,3,4} , and Garrett K. Keating⁵

¹ Département de Physique Théorique, Université de Genève, 24 quai Ernest Ansermet, 1211 Genève 4, Switzerland; Azadeh.MoradinezhadDizgah@unige.ch

² INFN, National Institute for Nuclear Physics, Via Valerio 2, I-34127 Trieste, Italy; emilio.bellini@ts.infn.it

³ IFPU, Institute for Fundamental Physics of the Universe, via Beirut 2, 34151 Trieste, Italy

⁴ SISSA, International School for Advanced Studies, Via Bonomea 265, 34136 Trieste, Italy

⁵ Center for Astrophysics, Harvard & Smithsonian, 60 Garden Street, Cambridge, MA 02138, USA

Received 2023 April 26; revised 2023 December 9; accepted 2024 January 10; published 2024 April 1

Abstract

Line intensity mapping (LIM) can provide a powerful means to constrain the theory of gravity and the nature of dark energy at low and high redshifts by mapping the large-scale structure over many redshift epochs. In this paper, we investigate the potential of the next generation ground-based millimeter-wavelength LIM surveys in constraining several models beyond Λ CDM, involving either a dynamic dark energy component or modifications of the theory of gravity. Limiting ourselves to two-point clustering statistics, we consider the measurements of auto-spectra of several CO rotational lines (from $J=2-1$ to $J=6-5$) and the [C II] fine structure line in the redshift range of $0.25 < z < 12$. We consider different models beyond Λ CDM, each one with different signatures and peculiarities. Among them, we focus on Jordan–Brans–Dicke and axion-driven early dark energy models as examples of well-studied scalar-tensor theories acting at late and early times, respectively. Additionally, we consider three phenomenological models based on an effective description of gravity at cosmological scales. We show that LIM surveys deployable within a decade (with $\sim 10^8$ spectrometer hours) have the potential to improve upon the current bounds on all considered models significantly. The level of improvements range from a factor of a few to an order of magnitude.

Unified Astronomy Thesaurus concepts: [Scalar-tensor-vector gravity \(1428\)](#); [Non-standard theories of gravity \(1118\)](#); [CO line emission \(262\)](#); [Line intensities \(2084\)](#)

1. Introduction

Deciphering the physics responsible for the observed current accelerated expansion of the Universe—and whether it is driven by a cosmological constant or a dynamical dark energy (DE) component, or results from modifications to Einstein’s theory of gravity (MG)—is one of the key open questions in modern cosmology. Shedding light on this question is the driving science case for several upcoming galaxy surveys, such as Euclid (Amendola et al. 2018) and DESI (Levi et al. 2019), which will map the large-scale structure (LSS) at redshifts $z \lesssim 2$ by measuring shape and clustering of galaxies. In the standard cosmological model (among others), DE is a subdominant component of the Universe’s energy density at redshifts $z \gtrsim 1$. That said, models with an increased density of DE at higher redshifts have been also considered in the literature. Examples include models with an early DE (EDE) component prior to recombination (e.g., Karwal & Kamionkowski 2016) that has attracted significant attention in recent years in the context of the Hubble tension (e.g., Poulin et al. 2019; Hill et al. 2020; Ivanov et al. 2020; Simon et al. 2023). In addition, there are also models exhibiting a “tracking behavior” at late times: the equation of state of DE $w(z)$ tracks the dominant component of the Universe in that particular epoch ($w \simeq 0$ during matter domination and $w \simeq -1$ for $z \lesssim 1$), so that their energy density at high redshifts is nonnegligible (e.g., Urena-Lopez & Matos 2000; Bassett et al. 2002; Rakhi & Indulekha 2009).

Beyond constraining possible modifications to the theory of gravity that can explain the current accelerated expansion, testing general relativity (GR) on cosmological scales is of significant interest and is highly complementary to constraints from the solar system and binary systems (Berti et al. 2015). Modifications to GR and a dynamic DE component can both modify the background expansion of the Universe and the growth of structure. Therefore, statistical properties of the LSS enable us to constrain the nature of gravity and DE.

Line intensity mapping (LIM) is emerging as a powerful probe of the LSS. In contrast to galaxy surveys that map the LSS by resolving individual galaxies, LIM relies on measuring cumulative spectral-line emission from an ensemble of galaxies or the intergalactic medium (Pritchard & Loeb 2012; Kovetz et al. 2017). The measurements of spatial fluctuations in the intensity of the spectral lines together with their precisely measured frequencies enable us to measure the expansion history and growth of structure over extended redshift epochs and a wide range of scales, largely inaccessible to traditional galaxy surveys. In addition to the 21 cm line of the hyperfine transition of neutral hydrogen, LIM at millimeter and submillimeter wavelengths, targeting spectral emission lines with rest-frame wavelengths in the far infrared (e.g., rotational lines of carbon monoxide $\text{CO}(J \rightarrow J-1)$; Righi et al. 2008; Lidz et al. 2011; Breyssse et al. 2014; Mashian et al. 2015; Li et al. 2016; Padmanabhan 2018) and fine structure of ionized carbon [C II] (Gong et al. 2011; Silva et al. 2015; Pullen et al. 2018; Padmanabhan 2019), has recently attracted growing attention both in the context of galaxy/star formation (Gong et al. 2011; Kovetz et al. 2019; Bernal & Kovetz 2022) and cosmology (Creque-Sarbinowski & Kamionkowski 2018;



Original content from this work may be used under the terms of the [Creative Commons Attribution 4.0 licence](#). Any further distribution of this work must maintain attribution to the author(s) and the title of the work, journal citation and DOI.

Karkare & Bird 2018; Moradinezhad Dizgah & Keating 2019; Moradinezhad Dizgah et al. 2019; Gong et al. 2020; Schaan & White 2021a, 2021b; Bernal et al. 2021, 2021; Liu & Breysse 2021; Scott et al. 2023). The wide array of pathfinder experiments such as CCAT-Prime (Chapman et al. 2022), COMAP (Cleary et al. 2022), CONCERTO (Ade et al. 2020b), COPSS (Keating et al. 2016), EXCLAIM (Ade et al. 2020a), mmIME (Keating et al. 2020), SPT-SLIM (Karkare et al. 2022b), and TIME (Crities et al. 2014) are paving the way for future wide-field surveys capable of providing high-precision constraints on cosmology by providing robust detections of the line intensity power spectrum and constraining the astrophysical model dependencies of the signal. Establishing the science cases for future surveys and determining optimized survey strategies to achieve relevant theoretical thresholds is of utmost importance.

Building upon our previous works investigating the potential of millimeter-wavelength LIM in constraining primordial non-Gaussianity (Moradinezhad Dizgah & Keating 2019; Moradinezhad Dizgah et al. 2019) and properties of neutrinos and light relics (Moradinezhad Dizgah et al. 2022a), in this paper we study the prospects for constraining DE and MG. Contrary to upcoming spectroscopic galaxy surveys mapping the LSS at redshifts $z \lesssim 2$, the broad redshift coverage of LIM observations enables us to map the background expansion and growth of structure both in the matter and DE domination epochs. As such, LIM surveys offer the possibility of testing the nature of DE or MG in the regime that has not been probed before. Furthermore, mapping the LSS on ultralarge scales allows searching for horizon-scale imprints of possible modifications of GR (see, e.g., Sailer et al. 2021; Berti et al. 2022; Scott et al. 2023; Casas et al. 2023 for recent studies on constraining beyond Λ CDM models with 21 cm and millimeter-wavelength LIM).

For this work, we consider a ground-based survey capable of probing six rotational lines of CO and [C II] over the redshift range of $0 < z < 12$, assuming the same survey characterizations as those used in Karkare et al. (2022a) and Moradinezhad Dizgah et al. (2022a). We analyze several beyond Λ CDM models that fall into two broad categories of *covariant* and *effective description* models. More specifically, we consider the Jordan–Brans–Dicke (JBD) theory of gravity and EDE driven by an ultralight axion (Poulin et al. 2019) as examples of *covariant* models. By contrast, within the *effective description*, we consider the Chevallier–Polarski–Linder (CPL) parameterization for the DE equation of state and two models for the effective description of luminal Horndeski theories. Lastly, in a hybrid approach, we consider an effective description of ShiftSymmetric Horndeski models imposing theoretical priors that ensure the consistency with the underlying *covariant theory*. This selection of models enables us to explore phenomenologically rather broad regions of the parameter space of viable models to determine the potential of future LIM surveys in constraining beyond Λ CDM scenarios.

In our forecasts, we use the LIMFISHER package, which will be publicly released upon publication of this paper. This code is written in C language and is designed to perform forecasts for LIM power spectra. It utilizes the CLASS Boltzmann solver (Blas et al. 2011) as well as its extensions for beyond Λ CDM models.⁶ In particular, we use the publicly available

CLASS_EDE code (Hill et al. 2020)⁷ for the EDE model, and the HI_CLASS code (Zumalacárregui et al. 2017; Bellini et al. 2018, 2020)⁸ for other models, including JBD, shift-symmetric Horndeski, and effective description of DE models. We only account for the imprints of the considered models at the linear level, as implemented in the Boltzmann codes, consistently neglecting nonlinear scales.

The rest of the paper is organized as follows. In Section 2, we review the theoretical models that we will consider, summarizing the model parameters and current bounds, as well as the imprints on the LSS. In Section 3, we describe the model of the power spectrum of line intensity fluctuations that we use in our forecasts. In Section 4, we summarize the Fisher forecast methodology, and in Section 5 we describe the survey specifications assumed in the forecasts. In Section 6, we present the results of the forecasts, and finally in Section 7 we draw our conclusions.

2. Review of Theoretical Models Beyond Λ CDM

In this section, we first lay out the theoretical framework for selecting the models to study and then review the main features of each of the models that we consider and their connection to the general framework, as well as the imprints of the model on the background evolution and the growth of structures.

We perform our analysis following two complementary approaches. To study alternative theories of gravity, it is common either to specify a covariant Lagrangian, in the following referred to as the *covariant approach*, or to build an *effective description* that encapsulates the effects of the additional degree of freedom on the evolution of perturbations on an FLRW background. The two approaches offer different advantages, and we use both to explore a meaningful portion of the parameter space of viable cosmological models.

Our starting point for the *covariant approach* is the following Lagrangian

$$\mathcal{L} = G_2(\phi, X) - G_3(\phi, X) + G_4(\phi)R + \mathcal{L}_m, \quad (1)$$

where \mathcal{L}_m is the matter Lagrangian, $G_{2,3}$ are functions of a scalar field ϕ and its canonical kinetic term $X \equiv -\dot{\phi}^{\mu}\dot{\phi}_{\mu}/2$, and G_4 is a function of the scalar field alone. This describes the sub-class of Horndeski models (Horndeski 1974; Deffayet et al. 2009; Kobayashi et al. 2011) with the additional requirement that the speed of gravitational waves (GWs) has to be equal to the speed of light (Baker et al. 2017; Creminelli & Vernizzi 2017; Ezquiaga & Zumalacárregui 2017; Sakstein & Jain 2017). This is why the G_4 function depends only on the scalar field and not on its derivatives; a derivative coupling, allowed in the full Horndeski framework, would modify the speed of gravitational waves. Our choice of this subclass of Horndeski models is driven by the near-simultaneous observation of the GW signal (GW17081) and the gamma-ray burst (GRB 170817A) emitted from the merger of a binary neutron star system, which established that the GW speed has to be equal to the speed of light within one part in 10^{15} (Abbott et al. 2017). Upon fixing the functional form of $G_{2,3,4}$ in Equation (1) and setting the initial conditions for the scalar field, it is possible to solve the background expansion history and the perturbations

⁶ https://github.com/lesgourg/class_public

⁷ https://github.com/mwt5345/class_edc

⁸ <http://hiclass-code.net>

consistently. However, for nonstandard choices of $G_{2,3,4}$, it is difficult to predict the evolution of the background and the perturbations.

An alternative approach that is not specific to a particular (covariant) Lagrangian is to utilize the “effective description” of dark energy, often denoted as Effective Field Theory for DE (EFTofDE). Here, the information content of Equation (1) can be compressed into a few meaningful functions of time (Gleyzes et al. 2013; Gubitosi et al. 2013; Bellini & Sawicki 2014). Up to linear order in perturbation theory (PT), the dynamics of Equation (1) can be fully described in terms of four⁹ functions of time¹⁰

$$\{w, \alpha_K, \alpha_B, M_*^2\}, \quad (2)$$

where $w \equiv p_{\text{DE}}/\rho_{\text{DE}}$ is the equation of state of DE that contributes to the expansion history of the Universe, while the remaining three functions affect only the evolution of the perturbations. In particular, α_K is the standard kinetic term of perfect fluids, α_B is the kinetic term arising from the coupling of the derivatives of the scalar field with the ones of the metric, and M_*^2 is an effective Planck mass squared characterizing the change in the strength of gravity.¹¹ One of the key advantages of this approach is that each one of these functions has a clear physical meaning, and they describe particular classes of models. In this scenario, one has the freedom of parameterizing these functions of time, keeping in mind that in Λ CDM they reduce to

$$\{w = -1, \alpha_K = 0, \alpha_B = 0, M_*^2 = 1\}. \quad (3)$$

The two approaches to modeling alternative theories of gravity are to some extent equivalent, but each one has its own peculiarities and is preferable in specific situations. The *covariant approach* is fully consistent; i.e., for a single theory it is possible to describe gravitational interactions in any regime. Still, it is not trivial to jump from one model to the other, and one needs some clever intuition to choose $G_{2,3,4}$. By contrast, the *effective description* is ideal for investigating general classes of models at once. It is closer to observations but can lead to nonphysical theories. Indeed, while any choice of the $G_{2,3,4}$ functions has a corresponding time evolution of $\{w, \alpha_K, \alpha_B, M_*^2\}$, it is not guaranteed that any time evolution of $\{w, \alpha_K, \alpha_B, M_*^2\}$ is the representation of a particular choice of $G_{2,3,4}$. The choice of approach depends on the needs of the analysis.

2.1. Jordan–Brans–Dicke

First, we study the constraints on the Jordan–Brans–Dicke (JBD) theory of gravity (Brans & Dicke 1961), the workhorse of modified gravity models extensively studied in the literature (e.g., Umiltà et al. 2015; Ballardini et al. 2016; Lima & Ferreira 2016; Joudaki et al. 2022). The JBD theory adds a new scalar degree of freedom with respect to GR that is not minimally coupled to the metric. Following the *covariant*

approach, JBD is recovered by specifying

$$G_2 = \frac{M_{\text{Pl}}^2}{\phi} \omega_{\text{BD}} X - V(\phi), \quad (4)$$

$$G_3 = 0, \quad (5)$$

$$G_4 = \frac{M_{\text{Pl}}^2}{2} \phi, \quad (6)$$

where $V(\phi)$ is a generic potential and ω_{BD} is the coupling constant of the theory. The GR limit is recovered when $\omega_{\text{BD}} \rightarrow \infty$. Therefore, the accelerated expansion of the Universe can be obtained for a sufficiently flat potential and a slow-rolling scalar field.

We restrict our analysis to a constant potential, i.e., $V(\phi) = \Lambda$ (see, e.g., Ballardini et al. 2016 for constraints on a power-law potential). Since Λ can be obtained by imposing that in a flat Universe the sum of the fractional densities has to be one, the free parameters of the theory are $\{\omega_{\text{BD}}, \text{IC}\}$, where IC stands for initial conditions of the scalar field. The initial value for the scalar field’s first derivative is irrelevant, since the scalar field evolves quickly to an attractor solution irrespective of the value of the first derivative. It is possible to recast the scalar field as an effective Newton’s constant using

$$\tilde{G}_{\text{eff}} = \frac{G_{\text{eff}}^{\text{today}}}{G} = \frac{4 + 2\omega_{\text{BD}}}{\phi(3 + 2\omega_{\text{BD}})}. \quad (7)$$

Then, the only two parameters that will be varied are

$$\{w_{\text{BD}}^{-1}, \tilde{G}_{\text{eff}}\}. \quad (8)$$

The strongest bounds on JBD gravity come from astrophysical probes. In particular, the stellar triple system PSR J0337 + 1715, where the inner pulsar–white dwarf binary is in orbit with another dwarf, was shown to provide the strongest bound on the market, i.e., $\omega_{\text{BD}} > 1.4 \times 10^5$ (95% CL; Archibald et al. 2018; Voisin et al. 2020). The current cosmological constraints are much weaker, i.e., $\omega_{\text{BD}} > 2230$ and $\tilde{G}_{\text{eff}} = 0.996 \pm 0.029$ (95% CL), from KiDSx2dFLenS, BOSS full-shape, Planck18, and Pantheon data (Joudaki et al. 2022). This is because the JBD model has no screening mechanism, which implies that the fifth force introduced by the scalar field at cosmological scales is not suppressed at small scales. Therefore, in the quest for the ultimate theory of gravity, JBD becomes less interesting than other competitors. However, it is still possible to use JBD to infer when cosmological probes will have the same constraining power as astrophysical probes. Furthermore, the JBD gravity is one of the few models that has survived the recent constraints from the neutron star merger that constrained the speed of gravitational waves. It is also worth noting that the constraints on the JBD gravity can, to some extent, give insights into the long-wavelength features of the generalized scalar-tensor theories (Avilez & Skordis 2014).

At the background level in JBD gravity, the scalar field begins to evolve during the radiation-dominated era as a power law of the scale factor. The expansion is slowed down during matter domination, and at late times the constant gravitational potential of the scalar field sources the accelerated expansion of the Universe. The scalar field evolution depends on the value of ω_{BD} ; the larger it is, the more frozen it is. Therefore, we expect strong degeneracies between the \tilde{G}_{eff} , the present-day Hubble parameter, H_0 , the total matter overdensity, Ω_m , and the amplitude of fluctuations $S_8 = \sigma_8 \sqrt{\Omega_m}$, as well as a relatively

⁹ Note that here we are considering a subclass of Horndeski. The full Horndeski theory requires five functions.

¹⁰ The derivative of the effective Planck mass M_*^2 is commonly written as $\alpha_M \equiv d \ln M_*^2 / d \ln a$.

¹¹ For more details on the properties of these functions, see, e.g., Bellini & Sawicki (2014).

mild correlation with the total sum of neutrino masses M_ν (see Joudaki et al. 2022 for a recent analysis).

2.2. Early Dark Energy Driven by Ultralight Axions

The models in which a new component acting as DE dominates the energy density of the Universe briefly before recombination and rapidly decays after the last scattering have recently attracted attention in the literature as a solution to alleviate the Hubble tension between the early and late Universe, as proposed originally in Karwal & Kamionkowski (2016). An EDE component increases the expansion rate, thus the value of H_0 , and acts to shrink the sound horizon at the last scattering. We consider the phenomenological model of EDE proposed in Poulin et al. (2019), which has been used in several recent analyses of the cosmic microwave background (CMB) and LSS data (see, e.g., Hill et al. 2020; Ivanov et al. 2020; Sailer et al. 2021) and got the silver medal in the H_0 Olympics (Schöneberg et al. 2022). This model envisages an ultralight axion, much lighter than fuzzy dark matter axions and displaced from the minimum of its potential at early times, as an EDE component and can be described in the *covariant approach* with

$$G_2 = M_{\text{Pl}}^2 X - m^2 f^2 \left[1 - \cos\left(\frac{\phi}{f}\right) \right]^n - \Lambda, \quad (9)$$

$$G_3 = 0, \quad (10)$$

$$G_4 = \frac{M_{\text{Pl}}^2}{2}. \quad (11)$$

Here, m is the axion mass, f is the axion decay constant, n is an exponent that generalizes the well-motivated axion-like potential (recovered by setting $n = 1$) and controls the rate of dilution after the field becomes dynamical, and Λ is a cosmological constant driving the late-time accelerated expansion of the Universe. Given that the dynamics are shown to be relatively insensitive to changes of $2 \lesssim n \lesssim 4.5$ (Smith et al. 2020; Agrawal et al. 2023), as done in previous analyses of Hill et al. (2020) and Schöneberg et al. (2022), we fix $n = 3$. Early on, due to Hubble friction, the axion stays in its displaced position and acts as an additional DE component. Once the Hubble parameter drops below the axion's mass ($H \lesssim m$), the field starts rolling down the potential and oscillates at its minimum. To have this EDE component dissipate fast and become a subdominant energy component, near the minimum, the potential should be steeper than quadratic. The physics of this model is, therefore, governed by three parameters,

$$\{f_{\text{EDE}}, \log_{10}(z_c), \theta_i\}, \quad (12)$$

where $f_{\text{EDE}} \equiv \max(\rho_{\text{EDE}}/3M_{\text{Pl}}^2 H^2)$, is the maximal fractional contribution of the EDE density to the total energy density of the Universe, z_c is the critical redshift at which this maximum is reached, and $\theta_i = \phi_i/f$ is the normalized initial value of the scalar field such that $-\pi < \theta_i < +\pi$.¹² Once f_{EDE} and z_c are fixed, the role of θ_i is to set the dynamics of perturbations right around z_c via EDE sound speed, c_s . The Λ CDM limit is recovered by setting the axion mass to zero in Equation (9).

This class of EDE models has been recently constrained using various combinations of data sets (e.g., Poulin et al. 2019; Hill et al. 2020; Smith et al. 2020; Schöneberg et al. 2022; Simon et al. 2023). We consider the results from Simon et al. (2023) and use the best-fit values as our fiducial model and their quoted 1σ errors as a baseline for comparison with our results,

$$f_{\text{EDE}} = 0.116_{-0.023}^{+0.027} \quad (13)$$

$$\log_{10}(z_c) = 3.83_{-0.15}^{+0.21} \quad (14)$$

$$\theta_i = 2.89_{-0.065}^{+0.19}. \quad (15)$$

We note that the above constraints are obtained from a joint analysis of Planck (temperature, polarization, and lensing) data and a BOSS full-shape galaxy power spectrum, imposing a prior on h_0 from SH0ES local distance-ladder data. Since our forecasts only include Planck priors (from temperature and polarization data) on Λ CDM and not on the EDE model, the comparison of LIM results with current constraints should be considered only a first exploration of the potential of LIM in constraining EDE.

To illustrate the potential of LIM data in constraining the EDE model, it is helpful to review the imprints of an EDE component on the clustering of matter and the biased tracers. The faster expansion rate before recombination in the EDE model implies a larger acoustic sound horizon at drag time, which shifts the peaks of Baryon Acoustic Oscillations (BAO) to smaller wavenumbers compared to the Λ CDM. The presence of an EDE field also affects the dynamics of the perturbations within the comoving horizon during the epochs in which EDE is relevant, slightly suppressing the growth of perturbations around the recombination. To have an EDE model consistent with the primary CMB power spectra, some of the Λ CDM parameters must shift: Ω_c is increased to compensate for the less efficient growth of perturbations, and n_s is increased since the EDE is only relevant in a short time period and its effect on perturbations is scale dependent. These parameter shifts alter the matter power spectrum, the effect (especially on smaller scales) being more prominent at higher redshifts. This redshift dependence is also encoded in the growth rate of the structure, which is measured via the redshift-space distortions (RSD) of galaxy clustering (Hill et al. 2020). In addition to modifications of the matter power spectrum, the halo/galaxy abundance and clustering can also be altered in the EDE scenario. Using N -body simulations, Klypin et al. (2021) showed that the halo mass function in the EDE model is enhanced compared to the Λ CDM model; i.e., the EDE model predicts more halos, with the enhancement being substantially more significant at higher redshifts and higher mass halos. Furthermore, halos of a given mass were shown to form earlier and have higher concentrations.¹³

Apart from mapping a larger number of modes and hence having a lower cosmic variance, having access to the wide range of spatial scales and redshifts makes LIM particularly powerful for constraining the EDE scenario. In terms of the scales, measuring the line power spectrum from horizon to nonlinear scales allows for constraints on the scale-dependent effect of the EDE (Hill et al. 2020). Access to large scales is

¹² The phenomenological parameters f_{EDE} and z_c are derived parameters obtained internally in the Boltzmann code by shooting on the original particle physics parameters m and f .

¹³ Despite the enhanced clustering of matter fluctuations in the EDE model resulting from a higher value of σ_8 , these results did not find higher clustering of halos in the EDE model.

crucial for models of EDE with lower critical redshifts since the growth suppression is pushed to later times, and thus affects correspondingly larger scales. For example, the EDE that peaks after recombination (not a viable resolution to the Hubble tension) suppresses the linear matter power spectrum in a scale-independent way on small scales and can only be probed via its effect on large scales (Sailer et al. 2021). Since the nonlinear gravitational evolution tends to reduce the difference between the EDE and Λ CDM models, probing higher redshifts is advantageous. Moreover, being sensitive to the halo mass function, the line signal picks up the imprint of the EDE on the halo abundance, which was shown to be substantial at high redshifts (Klypin et al. 2021).

2.3. Standard CPL Parameterization of Dark Energy

A simple and widely used description for DE models is the CPL parameterization (Chevallier & Polarski 2001; Linder 2003). It falls in the *effective description* category, and it assumes the presence of a DE fluid with the equation of state

$$w = w_0 + w_a(1 - a), \quad (16)$$

where w_0 is the value of the DE equation of state today, and w_a modulates its time dependence, with a being the scale factor. This fluid is a minimal extension of the standard cosmological model, which is recovered by setting $w_0 = -1$ and $w_a = 0$. The role of w is only to modify the expansion rate of the Universe, and it (mildly) affects the evolution of the perturbations only through a modified Hubble parameter (in the next Sections we will present present models that have intrinsic additional freedom for the perturbations). Recent constraints from the CMB, BAO, and supernovae (Aghanim et al. 2020) show that these parameters are compatible with the standard Λ CDM model; i.e.,

$$w_0 = -0.957 \pm 0.080, \quad (17)$$

$$w_a = -0.29^{+0.32}_{-0.26}. \quad (18)$$

In our forecasts we set the fiducial values of $w_0 = -1$ and $w_a = 0$ corresponding to Λ CDM. LIM can provide tight constraints on the CPL model by measuring the expansion history over a wide redshift range and thus, is expected to tightly constrain the redshift dependence of the DE equation of state, i.e., the w_a parameter.

2.4. Shift-symmetric Horndeski Models

To build a very general, yet tractable, MG theory from Equation (1), it is possible to assume that the scalar field is slowly evolving on a cosmological background and Taylor expand the $G_{2,3,4}$ functions for small X . To further compress the parameter space of the theory, we place constraints only on shift-symmetric models; i.e., models invariant under $\phi \rightarrow \phi + c$ (where c is some constant). Shift-symmetric theories are interesting because radiative corrections are parametrically suppressed around (quasi) de Sitter backgrounds (Luty et al. 2003; Nicolis et al. 2009). Following the *covariant approach*, a shift-symmetric version of Equation (1) expanded up to quadratic order in X looks like

$$G_2 = c_{01}X + \frac{c_{02}}{\Lambda_2^4}X^2, \quad (19)$$

$$G_3 = -\frac{1}{\Lambda_3^3} \left(d_{01}X + \frac{d_{02}}{\Lambda_2^4}X^2 \right), \quad (20)$$

$$G_4 = \frac{M_{\text{Pl}}^2}{2}, \quad (21)$$

where $\{c_{01}, c_{02}, d_{01}, d_{02}\}$ are parameters of the theory, and commonly it is assumed that $\Lambda_2^4 = M_{\text{Pl}}^2 H_0^2$ and $\Lambda_3^3 = M_{\text{Pl}} H_0^2$ to ensure that all interactions have $\mathcal{O}(1)$ contributions to present-day cosmological background evolution. This theory is a rather minimal, yet rich four-parameter extension of Λ CDM. However, instead of constraining the parameters of this theory, we follow an alternative and more powerful approach proposed in García-García et al. (2020) and Traykova et al. (2021), in which the parameter space of Equations (19)–(21) is projected into the *effective description*.¹⁴ In other words, they investigate how the *effective description* functions evolve with time if they are obtained consistently from Equations (19) to (21), instead of parameterizing them directly (as in the spirit of the *effective description* formalism). This provides theoretical priors on the *effective description* functions that ensure we are dealing with physical theories. The theoretical priors have to be interpreted as the region in the parameter space where a “covariant theory” will likely fall. A possible tension between data-driven constraints and theoretical priors would not indicate the data have preference on nonphysical theories, but rather that only a few of the physical theories are in agreement with data.

As anticipated, following the results of Traykova et al. (2021), we can safely ignore Equations (19)–(21) and study their proposed parameters, i.e.,

$$\{w_0, w_a, \hat{\alpha}_B, m\}, \quad (22)$$

which come from simple parameterizations of the *effective description* functions

$$w = w_0 + w_a(1 - a) \quad (23)$$

$$\alpha_B = \hat{\alpha}_B \left(\frac{aH_0}{H} \right)^{4/m}. \quad (24)$$

It is clear that $\hat{\alpha}_B$ represents the magnitude of α_B today, and the parameter m modifies its dependence on the Hubble parameter H . The Λ CDM limit is obtained fixing $w_0 = -1$, $w_a = 0$, and $\hat{\alpha}_B = 0$, in which case the value of m becomes irrelevant.

Combining observational constraints from the CMB, BAO, RSD, and supernovae Type IA data with theoretical priors, and assuming that the scalar field is entirely responsible for the late-time acceleration (case $\Lambda = 0$ in Traykova et al. 2021),¹⁵ in Traykova et al. (2021) they obtained the following constraints on the four model parameters

$$w_0 = -0.97 \pm 0.03, \quad (25)$$

$$w_a = -0.11 \pm 0.06, \quad (26)$$

$$\hat{\alpha}_B = 0.6 \pm 0.3, \quad (27)$$

¹⁴ García-García et al. (2020) present an in-depth treatment of quintessence models, while Traykova et al. (2021) show results for the model considered here.

¹⁵ This was dubbed the “self-accelerating” version of the shift-symmetric model, which in general is more restrictive and easier to rule out with observational data. In this case, G_2 is bounded to be negative; thus, it is the form of G_3 that restores a positive kinetic energy and avoids ghosts.

$$m = 2.4 \pm 0.4, \quad (28)$$

which we will use to set the fiducial values for our forecasts and as a comparison point for results.

As already mentioned, one of the advantages of the *effective description* is that different physical effects can be encapsulated by independent functions of time. These functions can thus be considered as orthogonal and treated separately. As described in Section 2.3, the DE equation of state, w , affects primarily the expansion rate of the Universe, which in turn modifies the growth of structures. Here, at the level of linear perturbations we have one more ingredient, which does not modify the expansion history but introduces a new scale dependence in the matter power spectrum. In particular, its amplitude is responsible for lowering the amplitude of the power spectrum at large scales ($k < 10^{-3} h \text{ Mpc}^{-1}$) and enhancing it at small scales.¹⁶ This effect is redshift dependent, being less evident at higher redshifts, and in general depends on the time evolution of α_B (regulated by the parameter m).

2.5. Effective Description of Luminal Horndeski Models

The last class of models we will investigate belongs to the *effective description* class of luminal Horndeski theories. Starting from Equation (2), we parameterize the four EFT functions as

$$w = w_0 + (1 - a)w_a \quad (29)$$

$$\alpha_K = a \quad (30)$$

$$\alpha_B = a \quad (31)$$

$$M_*^2 = 1 + c_M^{(0)} - c_M^{(1)}(1 - a) + c_M^{(2)}(1 - a)^2. \quad (32)$$

The kineticity α_K is largely unconstrained by cosmological data (Bellini et al. 2016), due to the building blocks of α_K being those of simple DE models with at most first derivatives in the scalar field Lagrangian. As a consequence, in the subhorizon limit, where terms with a higher number of spatial derivatives become dominant, the DE fluid becomes almost negligible. We additionally fix α_B in our forecast. Taking into account that its effect has been explored in Section 2.4 and to avoid excessively enlarging the parameter space, we focus on the remaining degree of freedom of luminal Horndeski theories, i.e., M_*^2 . It is also important to remember that by construction the *effective description* allows to separate the different physical effects, which makes it possible to study the effects of one single function at a time and then draw conclusions on the general model.¹⁷

We keep α_K and α_B fixed to the evolution of the scale factor while varying the parameters related to the expansion history and Planck mass, as is similarly done in Raveri et al. (2017), where

$$\{w_0, w_a, c_M^{(0)}, c_M^{(1)}, c_M^{(2)}\}. \quad (33)$$

This parameterization is a power-law expansion around the present epoch up to first order in the expansion history and second order in the effective Planck mass. It allows a smooth

Table 1

Summary of Models Considered in the Fisher Forecasts and Corresponding Free Parameters

Model	Parameters
JBD	$\omega_{\text{BD}}^{-1}, \tilde{G}_{\text{eff}}$ {800, 1}
Early-DE (ULA)	$f_{\text{EDE}}, \log_{10}(z_c), \theta_i$ {0.105, 3.59, 2.71}
CPL	$\{w_0, w_a\}$ {-1, 0}
ShiftSym-Horndeski	$w_0, w_a, \hat{\alpha}_B, m$ {-0.97, -0.11, 0.6, 2.4}
Effective-DE	$w_0, w_a, c_M^{(0)}, c_M^{(1)}, c_M^{(2)}$ model1: {-1, 1, 1, 1, 0} model2: {-1, 1, 1, -1, -2}

GR limit (i.e., where Equation (33) can be expressed as {-1, 0, 0, 0, 0}) and can have rich dynamics. While the vast majority of the models proposed in the literature as late-time DE/MG kick in at $z \sim 1$, we explore the potential of LIM experiments spanning a wide range of redshifts. Thus, we choose two ad hoc models (defined in Table 1), designed to have signatures at high redshift, i.e., $2 \lesssim z \lesssim 10$. In particular, the effective Planck mass of *model1* increases smoothly with time, and its deviations with respect to 1 are $\sim 10\%$ at $z = 10$. The *model2* is even more extreme, with deviations of $\sim 25\%$ at $z = 10$ but also a feature at $z \simeq 1$ after which M_*^2 starts decreasing.

Two types of information can be derived from forecasts on this model: (i) we can maximize the constraining power of LIM experiments on DE/MG parameters, and (ii) understand to what extent a time-varying effective Planck mass can be constrained in this regime. The effective Planck mass M_*^2 , together with its derivative α_M , enhances the growth of structures at large scales ($k \simeq 10^{-3} \text{ Mpc}^{-1} h$) while keeping the amplitude of the matter power spectrum almost constant at smaller scales. The effect is redshift dependent, and only models with high-redshift signatures will have the matter power spectrum modified at high redshift.

3. The Power Spectrum of Line Intensity Fluctuations

We use a simple model for the line intensity signal, in which line intensity is calculated via scaling relationships between host halo mass and the CO or [C II] luminosities of the galaxies. The details of the model and relevant references to previous works on modeling line power spectra can be found, e.g., in Moradinezhad Dizgah et al. (2022a). Here, we just give the final form of the line power spectrum used in our forecasts.

The total observed power spectrum of fluctuations in a given line has three contributions: clustering, shot noise, and instrumental noise,

$$P_{\text{tot}}(k, \mu, z) = P_{\text{clust}}(k, \mu, z) + P_{\text{shot}}(z) + P_N(k, z). \quad (34)$$

Here, μ is the cosine of the angle between wavevector \mathbf{k} and the line-of-sight direction. The clustering contribution (typically in units of $\mu K^2 \text{ Mpc}^{-3} h^3$) is anisotropic due to the RSD and the Alcock-Paczynski (AP) effect. Assuming linear bias, on large

¹⁶ See Figure 2 of Zumalacáregui et al. (2017) for an illustration of this point. Even though a different parameterization is used in this plot, its behavior is the same as the one we are considering.

¹⁷ Strictly speaking, this is valid only when the deviation of these functions with respect to their standard Λ CDM value is $\lesssim 1$ to be able to neglect quadratic terms.

scales the line power spectrum is given by

$$P_{\text{clust}}^s(k, \mu, z) = \frac{H_{\text{true}}(z)}{H_{\text{ref}}(z)} \left[\frac{D_{A,\text{ref}}(z)}{D_{A,\text{true}}(z)} \right]^2 \times [1 + \mu_{\text{true}}^2 \beta(k_{\text{true}}, z)]^2 \exp\left(-\frac{k_{\text{true}}^2 \mu_{\text{true}}^2 \sigma_v^2}{H^2(z)}\right) \times [\bar{T}_{\text{line}}(z)]^2 b_{\text{line}}^2(z) P_0(k_{\text{true}}, z), \quad (35)$$

where \bar{T} is the mean brightness temperature of the line, b_{line} is the linear bias of the line, P_0 is the linear matter power spectrum, H is the Hubble parameter, D_A is the comoving angular diameter distance, $\beta = f/b_{\text{line}}$, and $f = d \ln D / d \ln a$ is the logarithmic growth rate of structure with D being the growth factor and a the scale factor. The wavenumbers and angles in the true and reference cosmologies (characterizing the AP effect) are related as

$$k_{\text{true}} = k \left[(1 - \mu^2) \frac{D_{A,\text{ref}}^2(z)}{D_{A,\text{true}}^2(z)} + \mu^2 \frac{H_{\text{true}}^2(z)}{H_{\text{ref}}^2(z)} \right]^{1/2}, \quad \mu_{\text{true}} = \frac{k\mu}{k_{\text{true}}} \frac{H_{\text{true}}(z)}{H_{\text{ref}}(z)}. \quad (36)$$

The exponent σ_v in Equation (35) includes both the finger-of-god (FoG) effect and the intrinsic line width of individual emitters, both of which result in smearing of power on small scales.

The mean brightness temperature of the line (typically in units of μK) at redshift z is given by

$$\bar{T}_{\text{line}}(z) = \frac{c^2 p_{1,\sigma}}{2k_B \nu_{\text{obs}}^2} \int_{M_{\min}}^{M_{\max}} dM \frac{dn}{dM} \frac{L_{\text{line}}(M, z)}{4\pi \mathcal{D}_L^2} \left(\frac{dl}{d\theta} \right)^2 \frac{dl}{d\nu}, \quad (37)$$

where M_{\min} and M_{\max} are the minimum and maximum masses of the halos that host galaxies emitting in a given line, c is the speed of light, k_B is the Boltzmann factor, ν_{obs} is the observed frequency of the line, dn/dM is the halo mass function, L_{line} is the specific luminosity of the line-emitting galaxy located in a halo of mass M at redshift z , and \mathcal{D}_L is the luminosity distance. The terms $dl/d\theta$ and $dl/d\nu$ reflect the conversion from units of comoving lengths, l , to those of the observed specific intensity: frequency, ν , and angular size, θ . The parameter $p_{1,\sigma}$ accounts for scatter in the relations between star formation rate and specific luminosity with halo mass (Keating et al. 2016; Li et al. 2016), and is given by

$$p_{n,\sigma} = \int_{-\infty}^{\infty} dx \frac{10^{nx}}{\sqrt{2\pi} \sigma_{\text{line}}} e^{-x^2/2\sigma_{\text{line}}^2}, \quad (38)$$

with $n=1$ for the mean temperature and $n=2$ for the shot-noise contribution, as discussed below. We set the value of $\sigma_{\text{line}} = 0.37$ for both CO and [C II], corresponding to the fiducial model of Li et al. (2016) and in reasonable agreement with observational studies (Sargsyan et al. 2012; Carilli & Walter 2013; Speagle et al. 2014; Kamenetzky et al. 2016).

In the Poisson limit, the shot-noise contribution arising from the discrete nature of line emitters is given by

$$P_{\text{shot}}^s(z) = \frac{c^4 p_{2,\sigma}}{4k_B^2 \nu_{\text{obs}}^4} \int_{M_{\min}}^{M_{\max}} dM \frac{dn}{dM} \times \left[\frac{L_{\text{line}}(M, z)}{4\pi \mathcal{D}_L^2} \left(\frac{dl}{d\theta} \right)^2 \frac{dl}{d\nu} \right]^2. \quad (39)$$

We note that to obtain more realistic forecasts, the line power spectrum model used in this work should be improved to include nonlinearities in matter distribution, RSD, and line biasing. Furthermore, one should account for deviations from Poisson shot noise (Moradinezhad Dizgah et al. 2022b) and marginalize over these corrections in addition to the full set of bias parameters to obtain cosmological parameters. Including more free parameters allows us to consider smaller scales in the forecasts, but at a fixed small-scale cutoff would result in weakening of the constraints compared to the linear model (see, e.g., Sailer et al. 2021). We leave forecasts using a more complete model to future work.

4. Analysis Methodology

We use the Fisher forecast formalism to determine the constraining power of a ground-based millimeter-wavelength intensity mapping survey, probing CO rotational lines and the [C II] line. Our analysis framework is the same as that we used in our previous paper, Moradinezhad Dizgah et al. (2022a). Therefore, we only summarize the main features here and refer the reader to that work for further details. We note that we consider a data vector consisting of only auto power spectra of individual lines and neglect the cross-correlations between different lines both in the signal and the noise. On the one hand, accounting for the cross-correlations can degrade the constraints since it enhances the variance of power spectra of individual lines. On the other hand, including the cross- and auto-spectra of all the observed lines can improve the constraints by reducing the cosmic variance (McDonald & Seljak 2009; Seljak 2009). Furthermore, including the cross-correlations in the Fisher forecast can further improve the constraints by reducing the impact of interloper lines (Chen & Pullen 2022).

Binning the survey in redshift bins of 0.1 dex and neglecting correlations between redshift bins, for each emission line x , the total Fisher matrix is the sum of Fisher matrices of individual redshift bins,

$$F_{\alpha\beta}^x = \sum_i F_{\alpha\beta}^{x,i} \quad (40)$$

with the Fisher matrix in the i th redshift bin given by

$$F_{\alpha\beta}^{x,i} = V_i \int_{-1}^1 \int_{k_{\min}}^{k_{\max}} \frac{k^2 dk d\mu}{8\pi^2} \text{Var}^{-1}[P_{\text{obs}}^x(k, \mu, z)] \times \frac{\partial P_{\text{clust}}^x(k, \mu, z_i)}{\partial \lambda_\alpha} \frac{\partial P_{\text{clust}}^x(k, \mu, z_i)}{\partial \lambda_\beta}, \quad (41)$$

where λ are the model parameters that are varied, V_i is the volume of i th redshift bin extended between z_{\min} and z_{\max} and is proportional to the sky coverage of the survey, f_{sky} , while $\text{Var}^{-1}[P_{\text{line}}^x]$ is the variance of the line power spectrum. We include the noise due to interloper lines from lower and higher redshifts in the variance of the line of interest; these interloper

contributions—typically dominated by low-redshift CO—are assumed to be removable in the power spectrum domain (e.g., Cheng et al. 2016).

We set the fiducial Λ CDM parameter values to those from Planck 2018 data (Aghanim et al. 2020)¹⁸: $\ln(10^{10}A_s) = 3.0447$, $n_s = 0.96589$, $h = 0.6732$, $\Omega_{\text{cdm}} = 0.2654$, and $\Omega_b = 0.04945$. The fiducial values of free parameters of each of the theoretical models considered are described in Section 2. We assume three degenerate massive neutrino species for all forecasts and fix their total mass to $M_\nu = 0.06$ MeV. For the finger-of-god contribution, we set the fiducial value of $\sigma_{\text{FOG},0} = 250 \text{ km s}^{-1}$.

We fix the line bias and mean brightness temperature to their theoretical values, accounting for their cosmology dependence. For the combined results of LIM and Planck, we use the available Planck 2018 Monte Carlo Markov Chain for Λ CDM¹⁹ to compute the parameter covariances and the Fisher matrix, marginalizing over optical depth and assuming the CMB and LIM Fisher matrices are independent so they can be summed to obtain the joint constraints. A more consistent forecast including Planck and LIM data requires computing the Fisher matrices of the two observables for the same beyond Λ CDM model. The choices of minimum and maximum scales, $[k_{\text{min}}, k_{\text{max}}]$, and the modeling of interlopers are the same as in Moradinezhad Dizgah et al. (2022a). The list of the models that we consider in our analysis is given in Table 1.

In addition to marginalizing over nonlinear biases and corrections to the Poisson shot noise, to obtain a more realistic forecast the line mean brightness temperature, \bar{T} , should also be marginalized over. While in general considering a more extended parameter space degrades the constraints at a fixed small-scale cutoff, it also can offer advantages; at the linear level, the linear bias and \bar{T} are highly degenerate, with RSD only partially breaking the perfect degeneracy between these two parameters in an isotropic power spectrum (Barkana & Loeb 2005; McQuinn et al. 2006; Sailer et al. 2022). Considering nonlinearities can further alleviate this degeneracy. As mentioned earlier, we leave consideration of a more extended model of the LIM power spectrum to a future work.

5. Survey Specifications

In this section, we briefly summarize the survey specifications that we assume in our forecasts and refer to Moradinezhad Dizgah et al. (2022a) for a detailed description of the hypothetical next-generation millimeter-wave LIM survey and how those specifications translate into sensitivity estimates used in our forecasts.

The instrument noise contributing to the measured power spectrum, P_N , is given in terms of per-voxel noise, σ_N , of the original image cube as

$$P_N = \sigma_N^2 V_{\text{vox}}. \quad (42)$$

V_{vox} is the volume of individual voxels within the image cube, which can be further expressed as

$$V_{\text{vox}} = \Omega_{\text{vox}} \delta\nu \left(\frac{dl}{d\theta} \right)^2 \frac{dl}{d\nu}. \quad (43)$$

Here, Ω_{vox} and $\delta\nu$ are the solid angle and bandwidth covered by a single voxel, respectively.

The per-voxel noise is parameterized by *spectrometer hours*, τ_{sh} , as a proxy for the “level of effort” of an experiment. If the survey area is Ω_s , such that the number of independent pointings is given by $\Omega_s/\Omega_{\text{vox}}$, then we can express Equation (42) as

$$P_N = \frac{\Omega_s \sigma_{\text{NET}}^2 \delta\nu}{\eta_{\text{opt}}^2 \tau_{\text{sh}}} \left(\frac{dl}{d\theta} \right)^2 \frac{dl}{d\nu}, \quad (44)$$

where σ_{NET} is the noise-equivalent temperature (NET) of the detector (units of $\text{K} \cdot \sqrt{\text{s}}$), and η_{opt} is the optical efficiency of the instrument. In computing σ_{NET} , we assume that the spectrometer performance is close to being background limited, with the primary contributors to the instrument noise being atmospheric emission, with secondary contributions from the telescope emissivity and various astrophysical backgrounds (including Galactic dust and the CMB). Further details on the simulated spectrometer performance can be found in Moradinezhad Dizgah et al. (2022a).

We define an effective instrumental noise,

$$\tilde{P}_N(k, \mu, z) = \alpha_{\text{max}}^{-1}(k, \mu) \alpha_{\text{min}}^{-1}(k, \mu) P_N, \quad (45)$$

to account for attenuation of the signal due to the finite resolution of the instrument (α_{max}) and the finite redshift and angular coverage of the survey (α_{min}). The two attenuation factors are defined in terms of the largest and smallest recoverable modes in parallel and perpendicular to line-of-sight directions. The former is determined by the redshift and angular coverage of the survey, while the latter is set by the spectral resolution of the instrument and the diameter of the aperture (see Moradinezhad Dizgah & Keating 2019; Moradinezhad Dizgah et al. 2022a for the full description and explicit expressions).

For our analysis, we consider ground-based observations from an accessible observing site with excellent proven millimeter-wave observing conditions, such as the South Pole or the Atacama desert. Each spectrometer is assumed to be sensitive to the entire frequency range; i.e., each spectrometer can measure all individual spectral channels simultaneously.

We vary spectrometer hours over a wide range, starting with first-detection experiments and extending to larger-scale surveys that could be fielded in the next ten years. We set the lower bound to be comparable to the current-generation instruments, which feature ~ 50 spectrometers (Crites et al. 2014) and are capable of completing surveys of order 10^5 spectrometer hours. As described in Moradinezhad Dizgah et al. (2022a), for each model, we calculate the parameter constraints while varying f_{sky} and spectrometer hours to determine the optimal survey strategy. We compute the constraints both with and without the addition of the Planck priors on Λ CDM parameters (only the former ones are shown in Section 6).

For our analysis, we tabulate and report the results with and without interlopers—the latter representing the optimistic view that the interloper emission can be (nearly) perfectly removed by leveraging the information contained with multiple overlapping lines (e.g., Cheng et al. 2020), and the former representing the pessimistic view that no suppression of interloper “noise” would be possible.

¹⁸ Specifically, we use `base_plikHM_TTTEEE_lowl_lowE`.

¹⁹ <http://pla.esac.esa.int/pla/#cosmology>

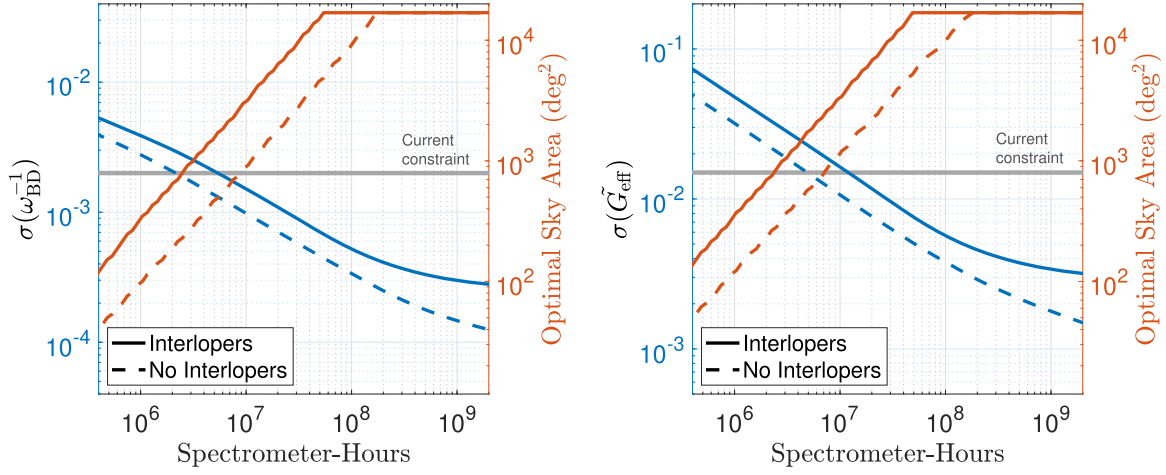


Figure 1. Blue lines show the 1σ constraints on JBD model parameters as a function of spectrometer hours, including (solid) and neglecting (dashed) interlopers. The red lines are the corresponding required sky coverage, and the gray bands are the existing constraints from a combination of KiDSx2dFLenS, BOSS full-shape, Planck18, and Pantheon data (Joudaki et al. 2022).

6. Results

In this section, we present the forecasted constraints for the models discussed in Section 2. For each model, we first describe the results of survey optimization by showing the marginalized constraints as a function of spectrometer hours and show the corresponding sky coverage required to achieve those constraints. In these plots, we show also a gray horizontal band, representing current constraints on each parameter. It is important to stress here that, when comparing the current constraints on the same parameter but for different models (e.g., w_0 from Sections 2.3 and 2.4) these can be different for two reason: (i) changes in the number of parameters, but most importantly (ii) the quoted current constraints come from different analyses that use different data sets. To illustrate the parameter degeneracies and the redshift dependence of the constraints for each model, we show the constraints on each parameter as a function of the maximum redshift, and the marginalized constraints on parameter pairs, assuming fixed spectrometer hours and sky coverage. Before discussing the results of individual models, let us summarize the main trends that are evident for all of them. Considering the dependence on survey parameters, the parameter constraint improves with increasing spectrometer hours and sky coverage. Accounting for interlopers degrades the constraints. For some parameters (which we discuss below), the degradation is most significant at higher values of spectrometer hours, causing saturation of the constraining power. This implies that in those cases, the noise from the interloper dominates the thermal noise determined by the number of spectrometer hours. Furthermore, the interloper noise pushes the required sky coverage to higher values. For all models, the redshifts corresponding to the peak of the star formation rate at which the amplitude of the line power spectrum is the largest ($z \sim 2$) provide considerable constraining power. However, the information content of the signal at different redshifts differs in the models considered, which we will discuss in what follows.

In Tables 2 and 3 of the Appendix, we show the 1σ marginalized constraints for all the considered models for five stages of LIM surveys defined in terms of an approximate number of spectrometer hours. For each model and each stage, we quote the constraints with (top row) and without (bottom row) interlopers.

6.1. Jordan–Brans–Dicke

In Figure 1, we show the 1σ constraints on parameters of the JBD model as a function of spectrometer hours, assuming the fiducial value of $\omega_{\text{BD}}^{\text{fid}} = 800$. The solid (dashed) blue lines show the constraints, including (neglecting) the interloper noise, and the red lines correspond to the required sky coverage to obtain those constraints. The plateau in the red lines corresponds to the maximum sky coverage of $f_{\text{sky}} \simeq 0.5$ that we have imposed. The gray bands are the current constraint from Joudaki et al. (2022).

For the comparison with the current bounds, it should be kept in mind that the JBD constraints (in particular ω_{BD}^{-1}) depend on the choice of fiducial values. Our choice of $\omega_{\text{BD}}^{\text{fid}} = 800$ is comparable to the peak of the 1d posterior of w_{BD}^{-1} in Joudaki et al. (2022). While only upper bounds on ω_{BD} are reported in Joudaki et al. (2022), the gray band we show here loosely corresponds to $\sigma(\omega_{\text{BD}}^{-1}) \sim 0.002$.

For $\lesssim 10^8$ spectrometer hours, the extra noise due to interlopers degrades the constraints on ω_{BD}^{-1} and \tilde{G}_{eff} by less than a factor of 2. At higher values of spectrometer hours, not removing the interlopers causes saturation of the constraining power as the interloper noise dominates the thermal noise. Furthermore, the unsubtracted interloper noise increases the required sky coverage by nearly a factor of 2; without interlopers the maximum sky coverage of 50% is saturated at $\sim 2 \times 10^8$ spectrometer hours, while with the interloper noise it is reached at $\sim 5 \times 10^7$ hours. Figure 2 shows the 1σ and 2σ marginalized constraints on parameter pairs to illustrate parameter degeneracies. Blue contours are from LIM only, while the red ones include Planck priors. As expected from the discussion in Section 2, for LSS probes, there are strong degeneracies between \tilde{G}_{eff} , h , and Ω_c (and to a lesser extent with Ω_b) due to their similar effects on the expansion rate and growth of structure. Imposing Planck priors improves the LIM-only results, both by tightening the constraints on Λ CDM parameters and by alleviating parameter degeneracies. We caution that while here we imposed Planck Λ CDM priors, a more careful joint analysis of the CMB and LIM, assuming the same model, is necessary to quantify the information content of the individual and combined probes more accurately.

Figure 3 shows the constraints as a function of maximum redshift z_{max} (top panel) and as a function of the center of each

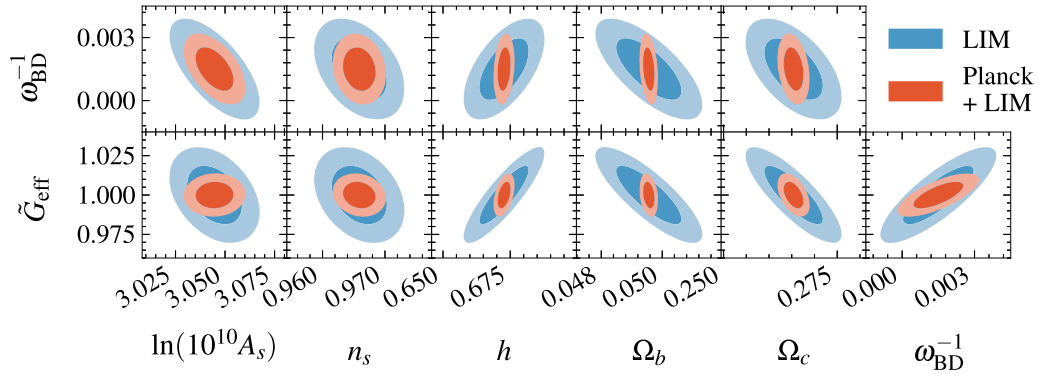


Figure 2. Marginalized 1σ and 2σ constraints on JBD and Λ CDM parameter pairs from LIM alone (blue) and when combined with Λ CDM Planck constraints (red). Interloper noise is included here, and the number of spectrometer hours is fixed to $\sim 10^8$.

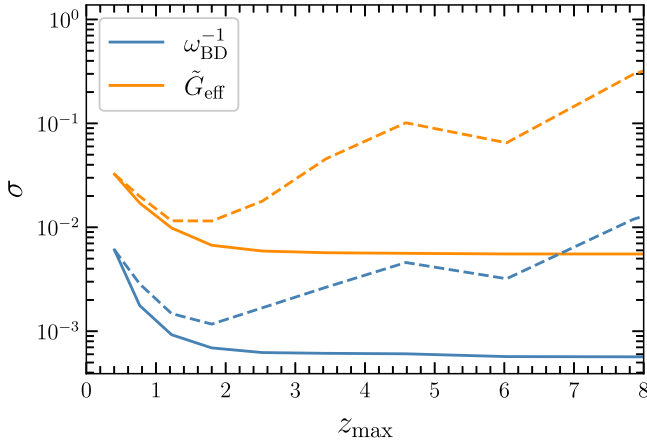


Figure 3. Solid lines show the marginalized 1σ constraints on the JBD model as a function of maximum redshift. For reference, we also show the constraints as a function of the center of redshift bins in dashed lines. Here, the interloper noise is accounted for, Planck priors are imposed, and the number of spectrometer hours is fixed to $\sim 10^8$.

redshift bin (bottom panel), assuming a fiducial value of $\omega_{\text{BD}} = 800$ and imposing Planck Λ CDM priors. For both parameters, the constraints improve with increasing z_{max} up to $z_{\text{max}} \sim 2.5$, after which a near plateau is reached. At $z \sim 6$ when the [C II] signal also contributes, we see a decrease of $\sim 15\%$ on $\sigma(\omega_{\text{BD}}^{-1})$, while $\sigma(\tilde{G}_{\text{eff}})$ is only lowered by 3%. At high redshifts, the survey we have considered here only has access to high- J rotational lines of CO, which are expected to be much fainter (in brightness temperature units) than their low- J counterparts. As a result, the constraints at $z \sim 6$ are primarily driven by [C II].

Comparing the constraints for fiducial values of $\omega_{\text{BD}}^{\text{fid}} = 800$ and $\omega_{\text{BD}}^{\text{fid}} = 10^5$, we find that the latter are tighter. To understand this behavior, it is important to stress that the larger the value of ω_{BD} is, the lesser the scalar field is evolving. In other words, in the limit $\omega_{\text{BD}} \rightarrow \infty$ the scalar field is completely frozen and reduces to a cosmological constant. Therefore, requiring a value of \tilde{G}_{eff} different than unity today would imply almost the same value at earlier times. That said, it is easier to accommodate deviations from $\tilde{G}_{\text{eff}} = 1$ for lower values of ω_{BD} , since an evolving scalar field would go back (in the past) to its tracker value ($\phi = 1$) rapidly. This is reflected also in the constraints of the other parameters. As an intuitive example, one could roughly think that the constraints on the parameters of the $\omega_{\text{BD}}^{\text{fid}} = 10^5$ model are the ones on the

$\omega_{\text{BD}}^{\text{fid}} = 800$ model, but fixing $\tilde{G}_{\text{eff}} = 1$ rather than marginalizing over it. Therefore, in comparing our results with previous forecasts, e.g., those of Alonso et al. (2017), the difference in the assumed fiducial values should be kept in mind.

6.2. Early Dark Energy Driven by Ultralight Axions

In Figure 4, we show the 1σ constraints on the three parameters of the EDE model as a function of spectrometer hours (in blue), and the corresponding sky coverage (in red). Again solid (dashed) lines show the results with (without) interloper noise, and the gray bands are the current constraints from Simon et al. (2023). As described in Section 2.2, in comparison of our results with existing bounds caution should be taken because the lack of Planck constraints on EDE parameters and the use of only Λ CDM priors makes our LIM + Planck constraints significantly more pessimistic. With this in mind, we see that the constraints on f_{EDE} can be improved significantly over the current bounds. By contrast, lowering the uncertainties for $\log_{10}(z_c)$ and in particular θ_i is more challenging, requiring a large number of spectrometer hours and larger sky coverage. In addition to the point above about the comparison with the current bounds, one can argue that the poor constraint on θ_i is also driven by the fact that the signature left by a change in its value, i.e., the normalized initial value of the scalar field, is erased by the proceeding evolution, mainly due to the EDE feature at recombination. For f_{EDE} and $\log_{10}(z_c)$, removing the interloper noise would allow a factor of $\sim (4-5)$ improvement over the current bounds for the $\sim 10^8$ spectrometer hours we considered, while the constraints on θ_i (without full Planck constraints) would be a factor of ~ 2 worse.

In Figure 5, we show the 1σ and 2σ marginalized constraints on parameter pairs. There are several degeneracies between EDE and Λ CDM parameters in LIM-only results in addition to those among the EDE parameters. The most notable ones are between f_{EDE} and Ω_b , A_s , and n_s , and between $\log_{10}(z_c)$, A_s , and n_s . Adding Planck priors on Λ CDM improves the constraints, in particular by tightening the constraints on Ω_b .

In Figure 6, we show the 1σ constraints as a function of maximum redshift z_{max} . Again, the trend is similar to that of the JBD model; constraints improve with increasing redshift up to $z_{\text{max}} \lesssim 2.5$. After that, the constraints almost completely plateau. Without imposing Planck priors (not shown in this plot), the constraint on $\log_{10}(z_c)$ improves by $\sim 14\%$ at $z_{\text{max}} \sim 6$, at which the [C II] signal is also included. Let us

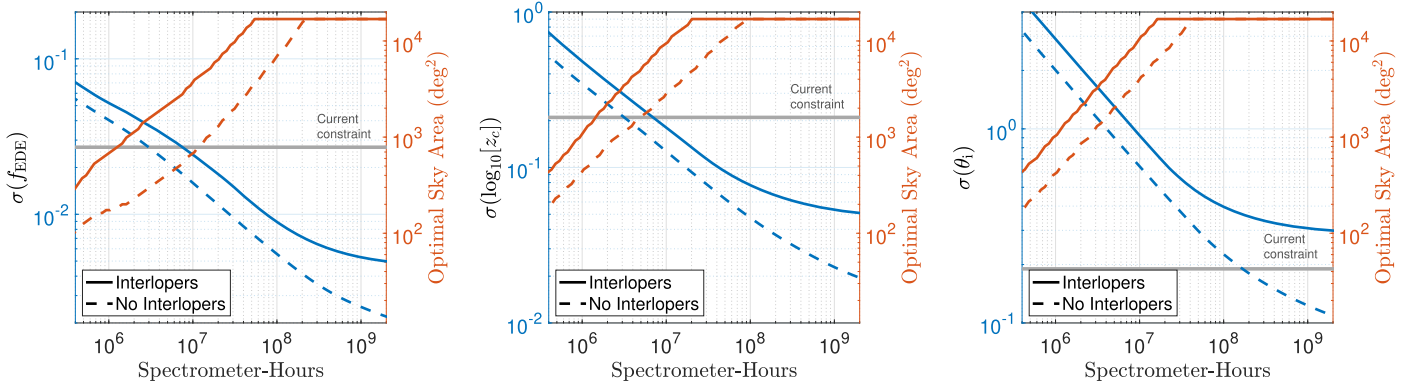


Figure 4. Blue solid (dashed) lines show the marginalized 1σ marginalized constraints on EDE driven by ultralight axions, including (neglecting) line interloper noise. The red lines show the corresponding required sky coverage, and the gray band shows the current bounds from Planck (temperature, polarization, and lensing) data and the BOSS full-shape galaxy power spectrum, imposing a prior on h_0 from the SH0ES local distance-ladder data (Simon et al. 2023). The Λ CDM Planck priors are applied.

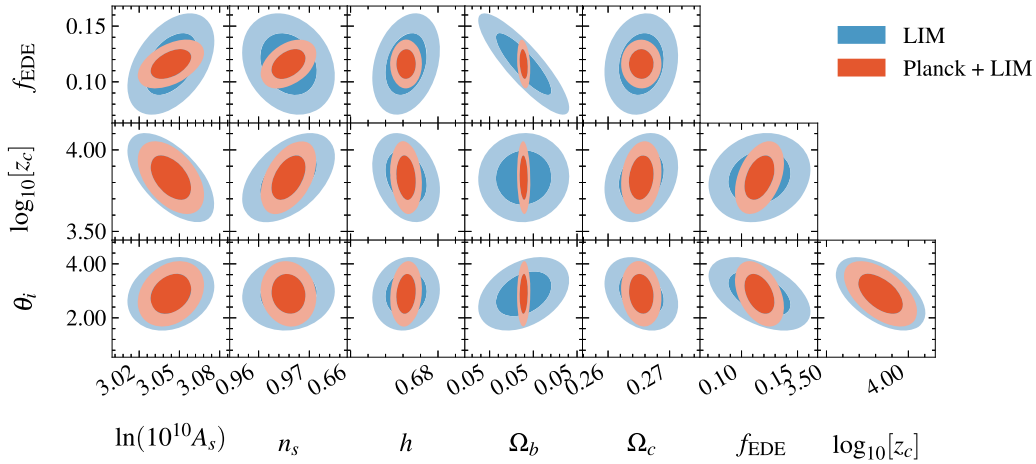


Figure 5. Marginalized 1σ and 2σ constraints on EDE and Λ CDM parameter pairs from LIM alone (blue) and when combined with Λ CDM Planck constraints (red). Interloper noise is included here, and the number of spectrometer hours is fixed to $\sim 10^8$.

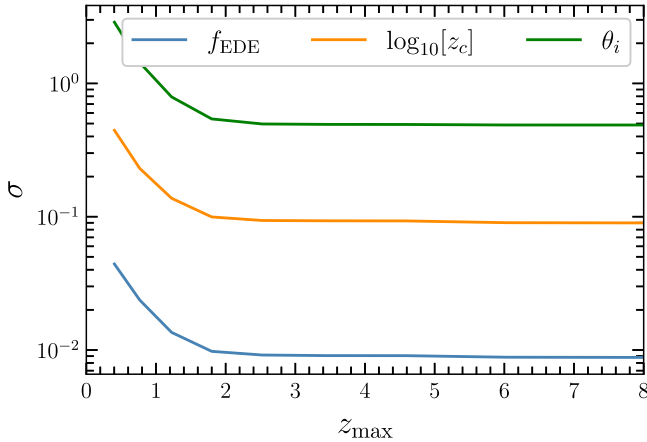


Figure 6. Marginalized 1σ constraints on EDE model parameters as a function of maximum redshift, including interloper lines, imposing Planck priors, and fixing the number of spectrometer hours to $\sim 10^8$.

emphasize that in interpreting the information content of LIM measurements at different redshifts some care should be taken. First, we have only included the effects of EDE on the linear matter power spectrum and modeled the line power spectrum at the linear level, and also did not include any modification to the halo mass function due to EDE (Klypin et al. 2021). Second,

for the survey specification that we have assumed, the thermal noise rapidly increases as we go to higher redshifts beyond $z \simeq 2.5$. Therefore, the fact that our results do not show a significant improvement beyond $z \simeq 2.5$ should not be taken as a strong statement about the constraining power of LIM measurements at high redshifts.

6.3. Standard CPL Parameterization of Dark Energy

In Figure 7, we show the results of the survey optimization for the CPL model, imposing Λ CDM Planck priors and including (solid) or neglecting (dashed) interlopers. Similar trends to other models are observed; i.e., improvement of constraints as a function of spectrometer hours, and a near power-law increase of the required sky coverage. The considered survey can provide significantly tighter constraints in the w_0 – w_a plane than the current bounds from the combination of the CMB, BAO, and supernovae (Aghanim et al. 2020). For $\sim 10^8$ spectrometer hours, and including the interloper noise, we obtain $\sigma(w_0) \sim 0.016$ and $\sigma(w_a) = 0.034$. As shown in Figure 7, even a relatively modest survey covering $\sim 10\%$ of the sky with $\sim 10^7$ spectrometer hours can improve the current bounds on w_0 and w_a by factors of about 2 and 3, respectively.

Figure 8 shows the 2D marginalized constraints on CPL and Λ CDM parameters with (red) and without (blue) Planck priors.

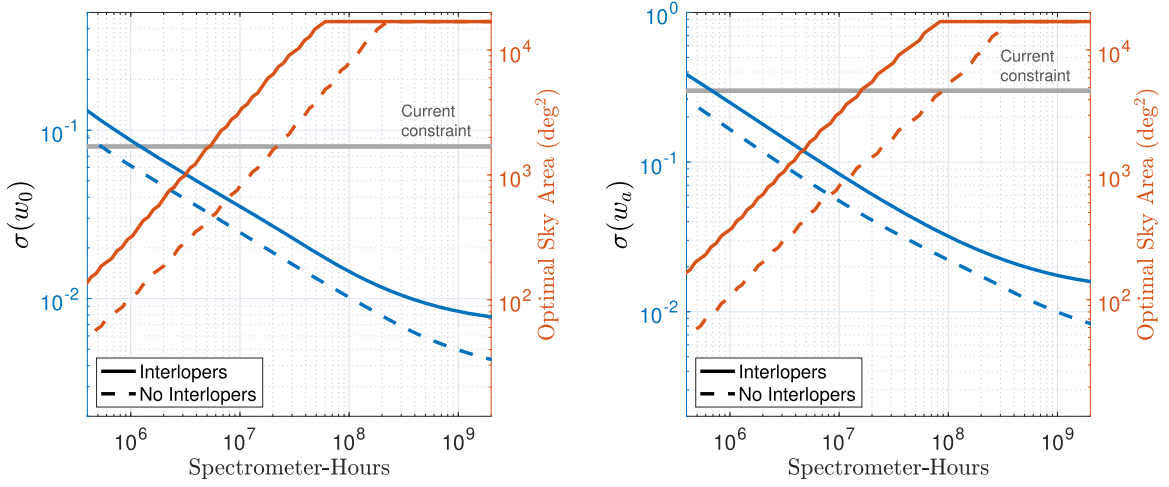


Figure 7. Blue solid (dashed) lines show the marginalized 1σ constrained and optimized survey configuration for CPL model, including (neglecting) interlopers, and imposing Planck priors on Λ CDM parameters. Red lines are the corresponding required sky coverage, and the gray bands are the current bounds from the CMB, BAO, and supernovae data.

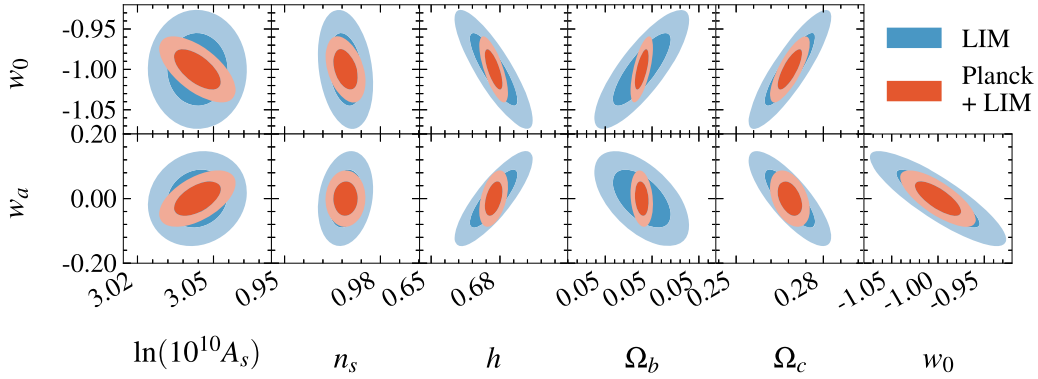


Figure 8. Marginalized 1σ and 2σ constraints on CPL and Λ CDM parameter pairs from LIM alone (blue) and when imposing Planck priors on Λ CDM parameters. Interloper noise is included here. The sky fraction is assumed to be $f_{\text{sky}} = 0.5$, and the number of spectrometer hours is fixed to $\sim 10^8$.

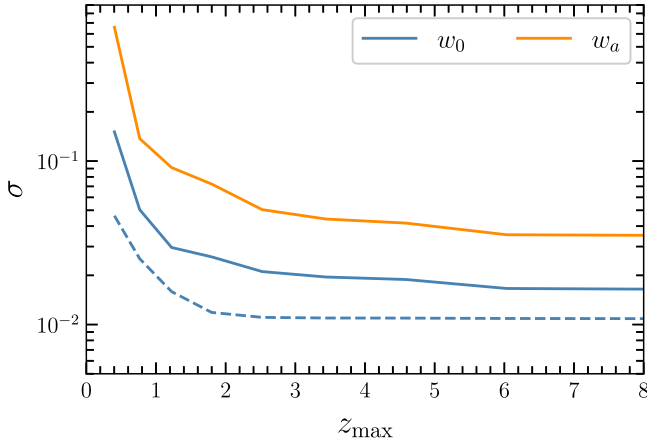


Figure 9. Marginalized 1σ constraints on the CPL model as a function of maximum redshift, including interloper noise, imposing Planck priors, and fixing the number of spectrometer hours to $\sim 10^8$. The dashed blue line shows the constraint on w_0 assuming a constant equation of state of DE.

There are strong degeneracies between w_0 and w_a , as well as between each of them and h , Ω_b , and Ω_c . Again, here, imposing Planck priors on Λ CDM improves the constraints on CPL parameters, primarily by tightening Λ CDM constraints. In an

actual joint analysis of the two data sets varying the same model, it is expected that breaking parameter degeneracies will also play essential role (see, e.g., Moradinezhad Dizgah et al. 2022a).

In Figure 9, we show the 1σ constraints on w_0 and w_a as a function of maximum redshift. We also show the constraint for the model with $w_a = 0$ in a dashed line to highlight the information gained by increasing z_{max} for the CPL model. While for a nondynamic DE there is no information gain at $z \gtrsim 1.8$, for the CPL model the constraints keep improving (only at the 5%–9% level in the redshift range of $2.5 < z_{\text{max}} < 6$). The addition of the [C II] signal at $z \sim 6$ improves constraints on both w_0 and w_a by about 20% and 25%, respectively.

Our results are comparable to the forecasts obtained for Euclid-like experiments. Blanchard et al. (2020) found that the 1σ errors on w_0 vary from 0.02 (optimistic scenario) to 0.04 (pessimistic scenario). This range of values improves current constraints and it is at the level of ours for an LIM experiment with $\sim 10^8$ spectrometer hours. The situation is a bit more favorable to LIM experiments for w_a , where their quoted constraints are 0.1–0.2. From the bottom panel of Figure 7 we notice that the next generation of LIM surveys improves easily these numbers, having a redshift excursion much higher than LSS surveys.

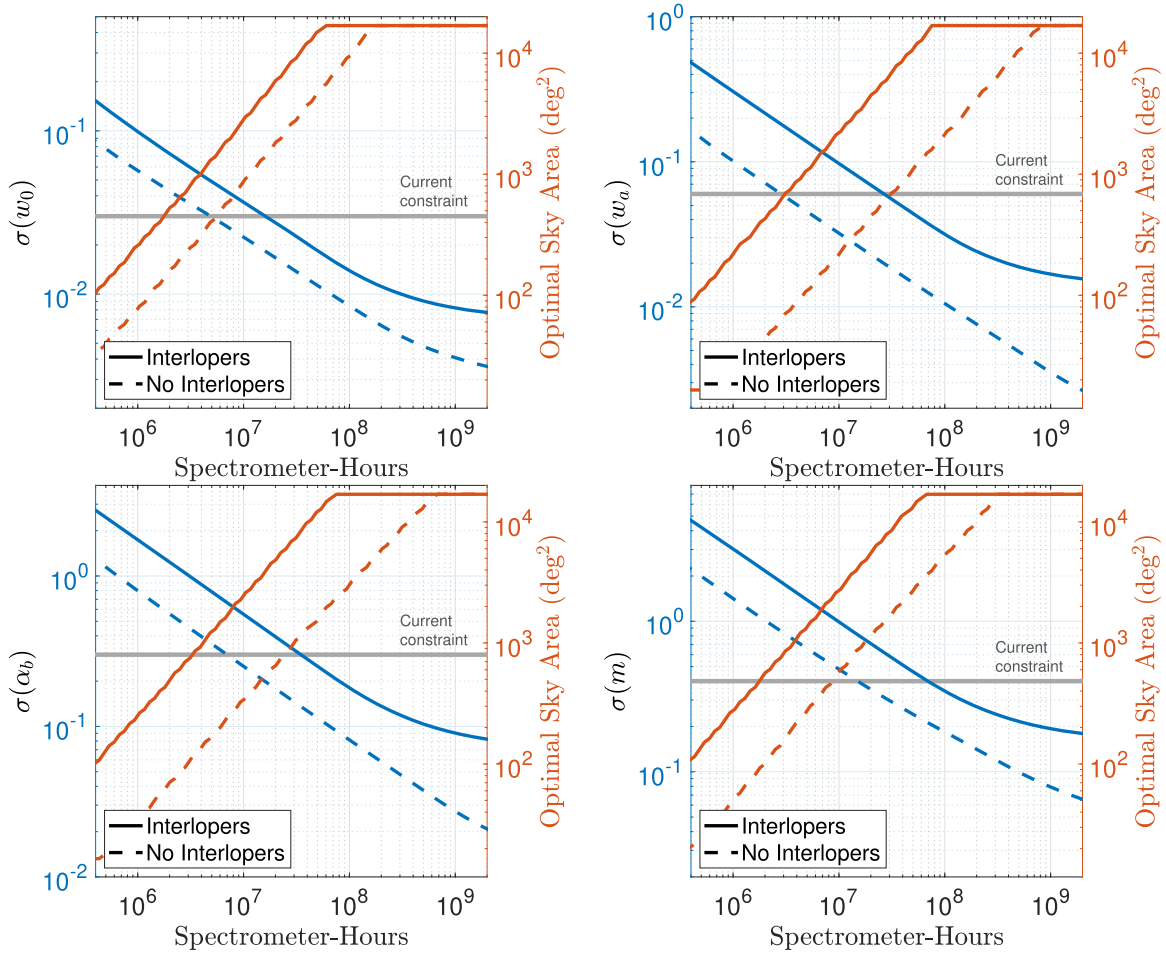


Figure 10. Blue solid (dashed) lines show marginalized 1σ constraints on background (top) and perturbation (bottom) parameters of the shift-symmetric Horndeski model, including (neglecting) interloper noise. Planck priors on Λ CDM parameters are imposed. Red lines are the corresponding required sky coverage and gray bands are the current bounds from the CMB, BAO, RSD, and supernovae Type IA data jointly with theoretical priors of Traykova et al. (2021).

6.4. Shift-symmetric Horndeski Models

In Figure 10, we show the results of survey optimization for the shift-symmetric Horndeski model, imposing the Planck priors and including (solid) or neglecting (dashed) interlopers. Comparing with the constraints on w_0 in this model with respect to the corresponding one for the pure CPL parameterization (shown in the top plot of Figure 7), we can see that the expected constraints with interlopers (solid blue lines) are essentially the same. This indicates that opening up the parameter space with $\hat{\alpha}_B$ and m does not degrade the constraining power of LIM experiments for the effective constant equation of state, as one would naively expect. This clearly suggests that the new parameter has orthogonal effects when considering LIM observables. It is also important to stress that what we quote here as the “current constraint” for w_0 is lower than the corresponding constraint for the CPL model in Section 6.3. This is simply due to the fact that in obtaining these constraints different data sets are used. A similar observation can also be made for w_a , with the only remarkable difference being that at low spectrometer hours its constraints here are slightly worse than in the previous analysis. This suggests that the constraining power of current LIM surveys leaves some degeneracy that broadens the allowed parameter space. Considering $\hat{\alpha}_B$, LIM alone will be able to improve the current constraints for $\gtrsim 4 \times 10^8$ spectrometer hours. With the

parameter m the situation is a bit different. First, the minimum spectrometer hours needed to improve the current constraints are 7×10^8 ; second, there is an almost-plateau at high spectrometer hours, which signals a diminishing return in pushing the survey specifications to their limits in constraining m .

Figure 11 shows the 1σ and 2σ marginalized constraints on the shift-symmetric Horndeski and Λ CDM parameter pairs, fixing the number of spectrometer hours to $\sim 10^8$. The LIM-only (blue) contours display strong degeneracies between w_0 and h , Ω_b , and Ω_c as in Figure 8. Also, w_a has a mild to large degeneracy with the same parameters. The degeneracy between w_0 and $(\hat{\alpha}_B, m)$ is removed when adding Planck priors, which tightly constrain h and Ω_b . The constraints on w_0 do not degrade with respect to CPL because the additional parameters are only mildly degenerate with w_0 when imposing Planck priors. Finally, it is worth noticing a strong degeneracy between $\hat{\alpha}_B$ and m , which is due to the fact that the time modulation parameterized by m can be reabsorbed into the overall amplitude $\hat{\alpha}_B$ for small redshift variations.

Figure 12 shows the marginalized 1σ constraints as a function of redshift. The improvements of the constraints for dynamical-DE parameters, w_0 and w_a , is significant up to $z \simeq 3.5$. Higher redshifts have little to no constraining power, similar to the other models. It is worth noticing that here the constraints saturate at higher redshifts with respect to those of

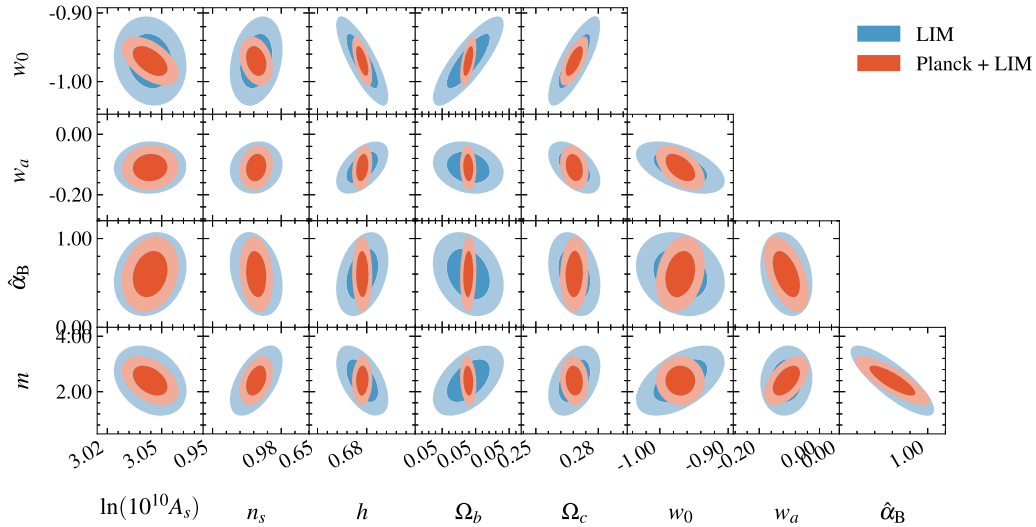


Figure 11. The 1σ and 2σ marginalized constraints on ShiftSym-Horndeski vs. Λ CDM parameters from LIM alone (blue) and when imposing Planck priors on Λ CDM parameters (red). Interloper noise is included here. The sky fraction is assumed to be $f_{\text{sky}} = 0.5$, and the number of spectrometer hours is fixed to $\sim 10^8$.

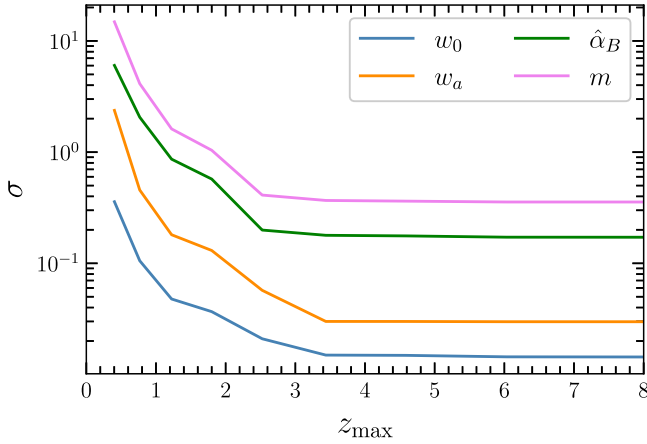


Figure 12. Marginalized 1σ constraints on ShiftSym-Horndeski model as a function of maximum redshift, including the interloper lines, imposing Planck priors, and fixing the number of spectrometer hours to $\sim 10^8$.

Figure 9. This is because we chose a different fiducial model. Instead of a pure Λ behavior, here we have an evolving DE component, which leaves clear imprints at higher redshifts. The saturation of the constraining power for $\hat{\alpha}_B$ and m is reached at a lower, but still large, redshift ($z \simeq 2.5$). It is easy to show that the time evolution of $\alpha_B(t)$ goes to zero more slowly than the most commonly considered models of MG/DE, which are designed to have low-redshift signatures.

6.5. Effective Description of Luminal Horndeski Models

The effective description of DE is, to some extent (as discussed in Section 2) the most general class of models we are investigating. On top of that, our fiducial models were designed ad hoc to have signatures beyond $z \simeq 1$ as normal dynamical-DE models. It is important to stress that the analysis of these models is meant to be illustrative of the potential of LIM surveys to probe general EFTofDE models, rather than to provide constraints on a specific model. Given our chosen parameterization, shown in Equation (23), constraints on this class of models provide insights into evolution of the DE equation of state, as well as time of the evolution of the Planck mass. As described in Section 2, both considered models are

designed to have signatures at high redshift, i.e., $2 \lesssim z \lesssim 10$. In particular, the effective Planck mass of *model1* increases smoothly with time, deviating from unity at the level of $\sim 10\%$ at $z \simeq 10$. The *model2* is even more extreme, with deviations of $\sim 25\%$ at $z \simeq 10$, but also a feature at $z \simeq 1$ after which the Planck mass starts decreasing.

Figure 13 shows the results of the survey optimization: the marginalized 1σ constraints as a function of spectrometer hours, together with the required sky coverage.²⁰ For all parameters, similar to all other models considered, the constraints improve as we increase the spectrometer hours. However, contrary to previous models, here removing the interlopers seems to be less important and we do not see saturation of the constraints in the range of spectrometer hours considered. This suggests that it should be possible (even if unrealistic with the next generation of surveys) to extract more information on these parameters by increasing the observation time. One notable difference between *model1* and *model2* (not shown here) is the role of the interloper lines: perfect removal of the interlopers does not considerably improve the constraints in *model2*, while it does for *model1*.

In Figure 14, we show the 1σ and 2σ marginalized constraints for *model1* (top panel) and *model2* (bottom panel). Without Planck priors, the degeneracies between background (w_0 or w_a) and perturbation parameters (c_M coefficients) are less severe in *model1* than in *model2*. We note that in *model1* the c_M coefficients are highly correlated with one another, while in *model2* only the degeneracy between $c_M^{(1)}$ and $c_M^{(0)}$ is significant. The degeneracy directions between $c_M^{(0)}$ and $c_M^{(1)}$ coefficients and w_0 and w_a in the two models are opposite one another. This is due the choices of fiducial values of the c_M coefficients in the two models. The constraint on $c_M^{(2)}$ in *model1* is significantly weaker than in *model2* due to its severe degeneracies with $c_M^{(0)}$ and $c_M^{(1)}$.

Figure 15 shows the marginalized 1σ constraints as a function of redshift for *model1* (left) and *model2* (right). While the perturbation parameters are better constrained in *model2*,

²⁰ While the plots refer to *model1*, most of the considerations that we are going to make are valid for *model2* as well. Whenever there are substantial differences between the results of the two models we will make it clear in the text.

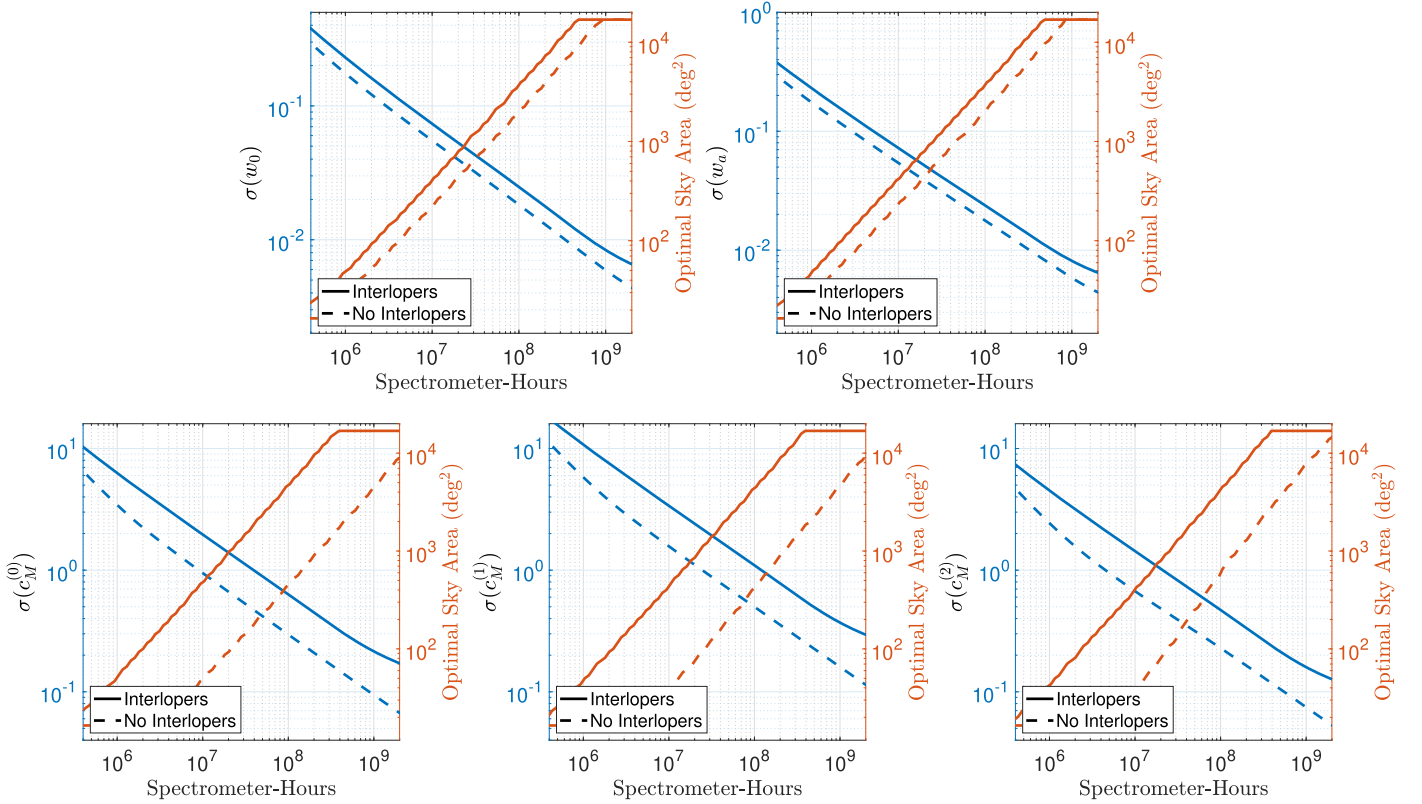


Figure 13. Blue solid (dashed) lines show marginalized 1σ constraints on background (top row) and perturbation (bottom row) parameters of the Effective-DE *modell*, including (neglecting) interloper noise. Red lines are the corresponding required sky coverage. Planck Λ CDM priors are imposed.

the constraints on background parameters are tighter in *modell*. The redshift dependencies of the constraints on w_0 and w_a are similar in both models, mostly saturating at $z \simeq 1.5$. For *model2* (right), the constraints on $c_M^{(2)}$ improve sharply (and by ~ 2 orders of magnitude) as a function of redshift. To interpret this result, one should take into account that the fiducial value for $c_M^{(2)}$ in *modell* was zero, while in *model2* we chose a value different from zero. This makes small variations around the fiducial model much more important in the second model.

7. Conclusion

Elucidating the nature of the DE component driving the current accelerated expansion and searching for possible modifications of gravity are two of major science goals for upcoming optical galaxy surveys. By offering the possibility of probing the LSS over a wide range of redshifts and scales, LIM can provide significant improvements in our understanding of the theory of gravity and the component of the Universe’s energy density acting as DE, in the regime largely beyond the reach of stage IV galaxy surveys.

In this paper, we performed Fisher forecasts to determine the potential of a hypothetical future multistage ground-based LIM survey, targeting several rotational lines of CO (from $J = 2-1$ to $J = 6-5$) and the fine structure line of [C II], in constraining several beyond Λ CDM models. The considered models include two classes: the first class are consistently described by a specific covariant Lagrangian for a scalar field such as Jordan–Brans–Dicke gravity and a (pre-recombination) early DE model. The second class are described in terms of an effective description of the evolution of the background and perturbations, without defining a Lagrangian. A hybrid approach has

been used for shift-symmetric Horndeski models. That is, instead of constraining the parameters appearing in the Lagrangian, we used the corresponding effective description. For each model, we varied two survey specifications, the number of spectrometer hours and the fraction of sky covered by the survey, and optimized the survey strategy to obtain the best parameter constraints minimizing the survey cost. We considered optimistic and pessimistic scenarios for removal of line interlopers versus accounting for them as a source of (anisotropic) noise, and obtained the parameter constraints with and without imposing Planck priors on Λ CDM parameters.

Our results show that for all models the considered LIM survey can improve upon the current bound by a factor of a few to an order of magnitude. We note that the optimal survey area does increase linearly with the number of spectrometer hours. However, the dependency of the parameter constraints on survey area is weak; thus, surveys with a wide range of sky coverage can provide results of similar magnitude. The interloper noise increases the required sky coverage to compensate for the additional noise contribution. Including the interloper lines degrades the constraints on all models but affects some parameters more significantly than others, causing a saturation of the parameter constraints even when increasing the number of spectrometer hours. Imposing Planck priors, thus tightening constraints on Λ CDM parameters, improves on beyond Λ CDM parameters, especially those most degenerate with them.

Among the models considered, for the JBD, the axion-driven EDE, and the CPL models, the constraints improve with increasing z_{\max} up to $z_{\max} = 2.5$, after which a near plateau is hit. The addition of a [C II] signal at $z \simeq 6$ can improve the constraints on some of the parameters by at most 15%–25%.

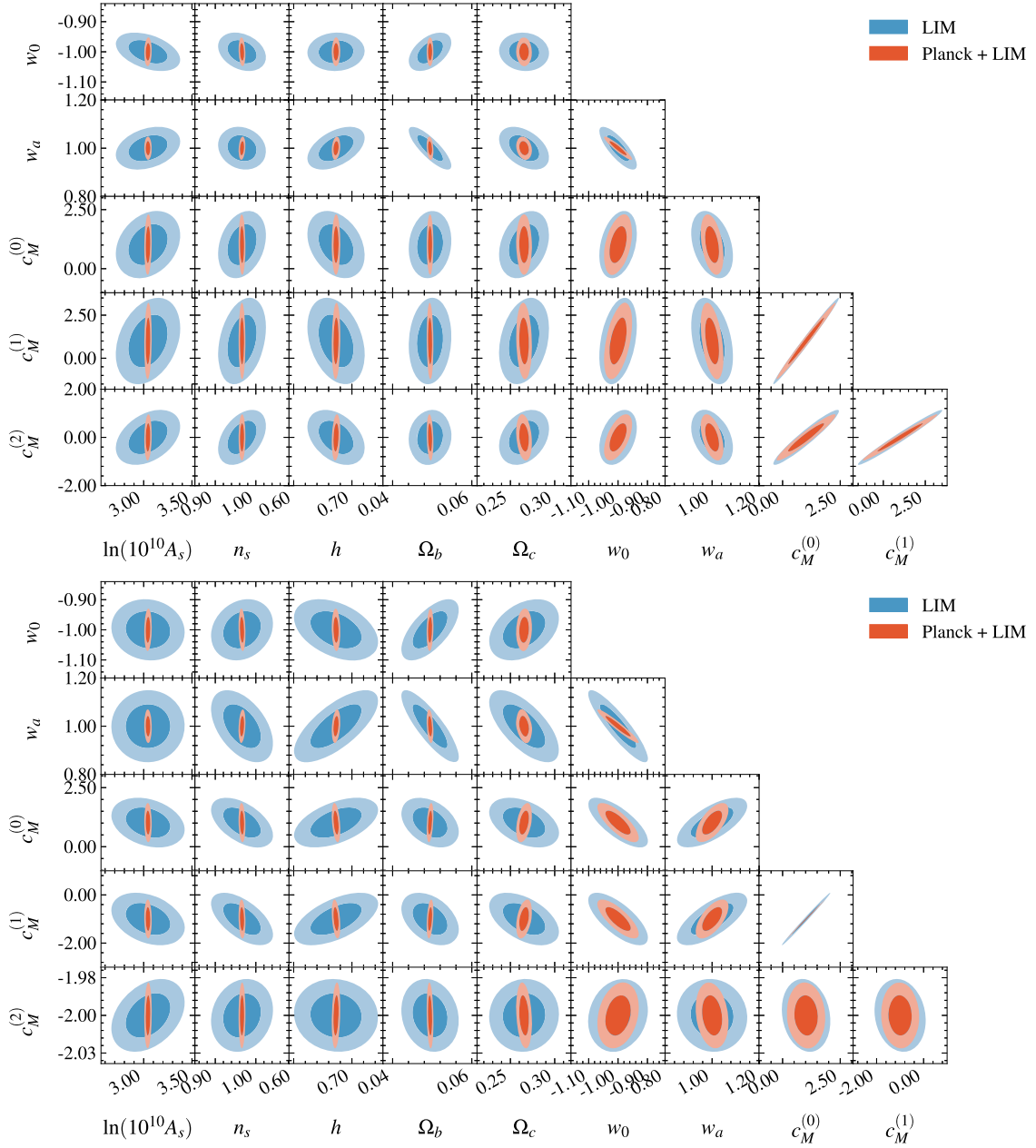


Figure 14. Marginalized 1σ and 2σ constraints on Effective-DE models and Λ CDM parameter pairs with (red) and without (blue) Planck Λ CDM priors. The top plot shows the constraints for *model1*, while the bottom one correspond to *model2*. Interloper noise is included here, and the number of spectrometer hours is fixed to $\sim 10^8$.

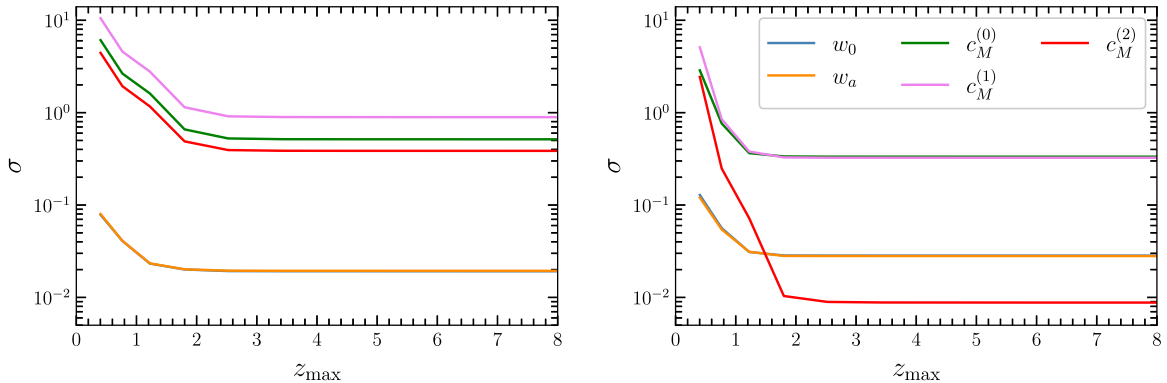


Figure 15. Marginalized 1σ constraints on Effective-DE *model1* (left) and *model2* (right) as a function of maximum redshift, including interloper noise, and imposing Planck priors. The curves for w_0 and w_a (in both plots) and curves for $c_M^{(0)}$ and $c_M^{(1)}$ (in the right plot) lie nearly completely on top of each other. Here, interloper noise is included, Planck Λ CDM priors are imposed, and the number of spectrometer hours is fixed to $\sim 10^8$.

For the shift-symmetric Horndeski model, the constraints on the DE equation of state keeps improving up to higher redshifts ($z_{\text{max}} \simeq 3.5$) and plateaus afterwards. For our selected effective description of luminal Horndeski models, the impact of interlopers does not lead to a saturation of the constraining power at high spectrometer hours, and instead just degrades the constraint by nearly constant factors. The interlopers affect the required sky coverage for best constraints on parameters describing the time evolution of the Planck mass more significantly than the DE equation-of-state parameters. We note that our assessment of the redshift dependence of the constraints is done under the pessimistic assumption that the interloper lines cannot be separated. However, in the optimistic case, we found upon further analysis that one can reap meaningful constraints from higher-redshift line emission. This further highlights the benefits from improved interloper separation.

It is worth noting that for several science goals considered in Section 6 a millimeter-wave LIM experiment begins to produce constraints that are competitive with current measurements at 10^7 spectrometer hours, concurrent with previous work focused on LIM-enabled constraints on neutrino properties (Moradinezhad Dizgah et al. 2022a). With a dedicated multiyear survey (with a total observing time of $\gtrsim 10^4$ hr), such a survey could be completed with a broadband camera of several dozen pixels—only a few times larger than LIM-focused instruments currently being deployed (e.g., Karkare et al. 2022b). As demonstrated, such surveys would optimally cover a survey area of a few thousand square degrees, well within the reach of current survey telescopes (e.g., SPT).

There are several directions in which this work can be extended. First, here we have assumed that the line bias and mean brightness temperature are perfectly predicted by the theory. In reality, given the uncertainty on the theoretical predictions of these parameters (e.g., due to uncertainty in the model of the line luminosity), one should marginalize over them. Second, since the variation of bias and mean brightness temperature is expected to degrade the constraints due to their degeneracies with cosmological parameters, studying how much the cross-correlations between different emission-line signals, as well as between LIM and galaxy clustering and the

CMB lensing, can ameliorate these degeneracies is of great interest. More generally, quantifying the potential improvements of the inferred constraints resulting from including both auto and cross-correlations is highly relevant. Third, in order to go beyond the Fisher forecasts, and in the absence of current wide-field LIM surveys, performing a likelihood analysis of mock LIM data, imposing Planck priors on the specific beyond Λ CDM models considered, is necessary. While here we have used Planck priors on Λ CDM parameters, a joint analysis of LIM and CMB primary anisotropies assuming the same model for the two is essential. Fourth, we have assumed a linear model of the line power spectrum and limited our analyses to relatively large scales. Including nonlinearities and promoting the model to include one-loop corrections, and marginalizing over a complete set of line biases is a natural next step. The improved model will allow us to go to smaller scales and potentially help to break the degeneracies between mean brightness temperature and linear line bias. Lastly, accurate characterization of foregrounds and observational systematics are crucial in obtaining more realistic forecasts.

Acknowledgments

It is our pleasure to thank David Alonso and Filippo Vernizzi for insightful discussions. A.M.D acknowledges funding from the Tomalla Foundation for Research in Gravity. E.B. has received funding from the European Union’s Horizon 2020 research and innovation program under the Marie Skłodowska-Curie grant agreement No. 754496.

Appendix Parameter Constraints for a Hypothetical Staged LIM Survey

Tables 2 and 3 show the 1σ parameter constraints for models described by a covariant approach and an effective parameterization, respectively. For each model, we show the constraints neglecting (top row) and including (bottom row) the interloper noise as optimistic and pessimistic cases. The number of spectrometer hours is representative of the timeline of the respective surveys, ranging from current-generation surveys ($\sim 10^5$ spectrometer hours) to those that can be envisioned in

Table 2
Stages of Future LIM Experiments and 1σ Marginalized Parameter Constraints for Models Described by a Covariant Lagrangian

Spec Hours	JBD		Early-DE			ShiftSymm-Horndeski			
	ω_{BD}^{-1}	\tilde{G}_{eff}	f_{EDE}	$\log_{10}(z_c)$	θ_i	w_0	w_a	$\hat{\alpha}_{\text{B}}$	m
10^5	0.00614	0.0953	0.0856	1.03	6.56	0.17	0.426	3.09	4.86
	0.00848	0.142	0.117	1.45	9.16	0.303	0.967	5.48	8.91
10^6	0.00277	0.0319	0.0404	0.345	2.01	0.0571	0.101	0.798	1.42
	0.00388	0.0479	0.052	0.482	2.9	0.099	0.305	1.74	3.03
10^7	0.000981	0.0106	0.0159	0.127	0.641	0.0223	0.0322	0.251	0.48
	0.00151	0.0163	0.0242	0.18	0.927	0.0367	0.0972	0.556	0.99
10^8	0.000338	0.00379	0.00555	0.0475	0.226	0.00847	0.0105	0.0814	0.184
	0.000522	0.00569	0.00892	0.077	0.397	0.0139	0.0316	0.18	0.343
10^9	0.000147	0.00178	0.00254	0.0229	0.123	0.00408	0.00354	0.0273	0.0792
	0.000299	0.0034	0.0053	0.0535	0.308	0.00823	0.0168	0.0904	0.193

Note. All numbers include Planck Λ CDM priors. The fiducial values for the parameters are given in Section 2. For each choice of spectrometer hours, the top row shows the constraints neglecting interlopers in the noise, while the bottom row includes the interlopers. See Table 2 of Moradinezhad Dizgah et al. (2022a) for approximate examples of the class of instrument required for each stage of the surveys.

Table 3
Same as Table 2, But for Models based on the Effective Description of DE

Spec Hours	CPL		Effective-DE, Model1					Effective-DE, Model2				
	w_0	w_a	w_0	w_a	$c_M^{(0)}$	$c_M^{(1)}$	$c_M^{(2)}$	w_0	w_a	$c_M^{(0)}$	$c_M^{(1)}$	$c_M^{(2)}$
10^5	0.199	0.604	0.781	0.773	19.9	34.2	14.5	1.21	1.16	13.1	12.8	0.48
	0.28	0.793	0.901	0.891	24.3	41.8	17.6	1.38	1.32	14.8	14.5	0.434
10^6	0.0668	0.182	0.175	0.175	3.44	5.81	2.44	0.257	0.247	2.75	2.68	0.0625
	0.0943	0.273	0.23	0.23	6.29	10.8	4.52	0.338	0.325	3.66	3.59	0.102
10^7	0.027	0.0603	0.0551	0.0542	0.947	1.57	0.672	0.0791	0.0759	0.887	0.863	0.0163
	0.0382	0.0908	0.0734	0.0723	1.96	3.38	1.43	0.106	0.101	1.18	1.15	0.032
10^8	0.011	0.0239	0.0183	0.0178	0.296	0.499	0.229	0.0262	0.0251	0.302	0.293	0.0055
	0.0157	0.0342	0.0248	0.0238	0.632	1.1	0.47	0.0356	0.0335	0.403	0.391	0.0105
10^9	0.00537	0.0109	0.00592	0.00585	0.0941	0.16	0.0746	0.00853	0.00826	0.0985	0.0955	0.0018
	0.00917	0.0189	0.00837	0.00813	0.215	0.4	0.159	0.0119	0.0112	0.141	0.137	0.00345

the next decade ($\sim 10^9$ spectrometer hours). The corresponding sky converge is obtained from optimization of survey strategy. Further details on survey specifications can be found in Moradinezhad Dizgah et al. (2022a).

ORCID iDs

Azadeh Moradinezhad Dizgah  <https://orcid.org/0000-0001-8841-9989>

Emilio Bellini  <https://orcid.org/0000-0003-4762-0795>

Garrett K. Keating  <https://orcid.org/0000-0002-3490-146X>

References

- Abbott, B. P., Abbott, R., Abbott, T. D., et al. 2017, *ApJL*, **848**, L13
- Ade, P. A. R., Anderson, C. J., Barrentine, E. M., et al. 2020a, *JLTP*, **199**, 1027
- Ade, P., Aravena, M., Barria, E., et al. 2020b, *A&A*, **642**, A60
- Aghanim, N., Akrami, Y., Ashdown, M., et al. 2020, *A&A*, **641**, A6
- Agrawal, P., Cyr-Racine, F.-Y., Pinner, D., & Randall, L. 2023, *PDU*, **42**, 101347
- Alonso, D., Bellini, E., Ferreira, P. G., & Zumalacárregui, M. 2017, *PhRvD*, **95**, 063502
- Amendola, L., Appleby, S., Avgoustidis, A., et al. 2018, *LRR*, **21**, 2
- Archibald, A. M., Gusinskaia, N. V., Hessels, J. W. T., et al. 2018, *Natur*, **559**, 73
- Avilez, A., & Skordis, C. 2014, *PhRvL*, **113**, 011101
- Baker, T., Bellini, E., Ferreira, P. G., et al. 2017, *PhRvL*, **119**, 251301
- Ballardini, M., Finelli, F., Umiltà, C., & Paoletti, D. 2016, *JCAP*, **05**, 067
- Barkana, R., & Loeb, A. 2005, *ApJL*, **624**, L65
- Bassett, B. A., Kunz, M., Silk, J., & Ungarelli, C. 2002, *MNRAS*, **336**, 1217
- Bellini, E., Cuesta, A. J., Jimenez, R., & Verde, L. 2016, *JCAP*, **02**, 053
- Bellini, E., & Sawicki, I. 2014, *JCAP*, **07**, 050
- Bellini, E., Sawicki, I., & Zumalacárregui, M. 2020, *JCAP*, **02**, 008
- Bellini, E., Barreira, A., Frusciante, N., et al. 2018, *PhRvD*, **97**, 023520
- Bernal, J. L., Caputo, A., & Kamionkowski, M. 2021, *PhRvD*, **103**, 063523
- Bernal, J. L., Caputo, A., Villaescusa-Navarro, F., & Kamionkowski, M. 2021, *PhRvL*, **127**, 131102
- Bernal, J. L., & Kovetz, E. D. 2022, *A&ARv*, **30**, 5
- Berti, E., Barausse, E., Cardoso, V., et al. 2015, *CQGr*, **32**, 243001
- Berti, M., Spinelli, M., Haridasu, B. S., Viel, M., & Silvestri, A. 2022, *JCAP*, **01**, 018
- Blanchard, A., Camera, S., Carbone, C., et al. 2020, *A&A*, **642**, A191
- Blas, D., Lesgourgues, J., & Tram, T. 2011, *JCAP*, **07**, 034
- Brans, C., & Dicke, R. H. 1961, *PhRv*, **124**, 925
- Breyse, P. C., Kovetz, E. D., & Kamionkowski, M. 2014, *MNRAS*, **443**, 3506
- Carilli, C., & Walter, F. 2013, *ARA&A*, **51**, 105
- Casas, S., Carucci, I. P., Pettorino, V., Camera, S., & Martinelli, M. 2023, *PDU*, **39**, 101151
- Chapman, S. C., Huber, A. E., Sinclair, A. K., et al. 2022, *Proc. SPIE*, **12190**, 1219005
- Chen, C., & Pullen, A. R. 2022, *MNRAS*, **512**, 4262
- Cheng, Y.-T., Chang, T.-C., Bock, J., Bradford, C. M., & Cooray, A. 2016, *ApJ*, **832**, 165
- Cheng, Y.-T., Chang, T.-C., & Bock, J. J. 2020, *ApJ*, **901**, 142
- Chevallier, M., & Polarski, D. 2001, *IJMPD*, **10**, 213
- Cleary, K. A., Borowska, J., Breyse, P. C., et al. 2022, *ApJ*, **933**, 182
- Cremineilli, P., & Vernizzi, F. 2017, *PhRvL*, **119**, 251302
- Creque-Sarbinowski, C., & Kamionkowski, M. 2018, *PhRvD*, **98**, 063524
- Crites, A. T., Bock, J. J., Bradford, C. M., et al. 2014, *Proc. SPIE*, **9153**, 91531W
- Deffayet, C., Deser, S., & Esposito-Farese, G. 2009, *PhRvD*, **80**, 064015
- Ezquiaga, J. M., & Zumalacárregui, M. 2017, *PhRvL*, **119**, 251304
- García-García, C., Bellini, E., Ferreira, P. G., & Traykova, D. 2020, *PhRvD*, **101**, 063508
- Gleyzes, J., Langlois, D., Piazza, F., & Vernizzi, F. 2013, *JCAP*, **08**, 025
- Gong, Y., Chen, X., & Cooray, A. 2020, *ApJ*, **894**, 152
- Gong, Y., Cooray, A., Silva, M. B., Santos, M. G., & Lubin, P. 2011, *ApJL*, **728**, L46
- Gubitosi, G., Piazza, F., & Vernizzi, F. 2013, *JCAP*, **02**, 032
- Hill, J. C., McDonough, E., Toomey, M. W., & Alexander, S. 2020, *PhRvD*, **102**, 043507
- Horndeski, G. W. 1974, *IJTP*, **10**, 363
- Ivanov, M. M., McDonough, E., Hill, J. C., et al. 2020, *PhRvD*, **102**, 103502
- Joudaki, S., Ferreira, P. G., Lima, N. A., & Winther, H. A. 2022, *PhRvD*, **105**, 043522
- Kamenetzky, J., Rangwala, N., Glenn, J., Maloney, P. R., & Conley, A. 2016, *ApJ*, **829**, 93
- Karkare, K. S., & Bird, S. 2018, *PhRvD*, **98**, 043529
- Karkare, K. S., Moradinezhad Dizgah, A., Keating, G. K., Breyse, P., & Chung, D. T. 2022a, arXiv:2203.07258
- Karkare, K. S., Andreson, A. J., Barry, P. S., et al. 2022b, *JLTP*, **209**, 758
- Karwal, T., & Kamionkowski, M. 2016, *PhRvD*, **94**, 103523
- Keating, G. K., Marrone, D. P., Bower, G. C., & Keenan, R. P. 2020, *ApJ*, **901**, 141
- Keating, G. K., Marrone, D. P., Bower, G. C., et al. 2016, *ApJ*, **830**, 34
- Klypin, A., Poulin, V., Prada, F., et al. 2021, *MNRAS*, **504**, 769
- Kobayashi, T., Yamaguchi, M., & Yokoyama, J. 2011, *PhThPh*, **126**, 511
- Kovetz, E. D., Viero, M., Lidz, A., et al. 2017, arXiv:1709.09066
- Kovetz, E. D., Breyse, P. C., Lidz, A., et al. 2019, *BAAS*, **51**, 101
- Levi, M. E., Allen, L. E., Raichoor, A., et al. 2019, *BAAS*, **51**, 57
- Li, T. Y., Wechsler, R. H., Devaraj, K., & Church, S. E. 2016, *ApJ*, **817**, 169
- Lidz, A., Furlanetto, S. R., Oh, S. P., et al. 2011, *ApJ*, **741**, 70
- Lima, N. A., & Ferreira, P. G. 2016, *JCAP*, **01**, 010
- Linder, E. V. 2003, *PhRvL*, **90**, 091301
- Liu, R. H., & Breyse, P. C. 2021, *PhRvD*, **103**, 063520
- Luty, M. A., Poratti, M., & Rattazzi, R. 2003, *JHEP*, **09**, 029
- Mashian, N., Sternberg, A., & Loeb, A. 2015, *JCAP*, **1511**, 028
- McDonald, P., & Seljak, U. 2009, *JCAP*, **10**, 007
- McQuinn, M., Zahn, O., Zaldarriaga, M., Hernquist, L., & Furlanetto, S. R. 2006, *ApJ*, **653**, 815
- Moradinezhad Dizgah, A., & Keating, G. K. 2019, *ApJ*, **872**, 126
- Moradinezhad Dizgah, A., Keating, G. K., & Fialkov, A. 2019, *ApJL*, **870**, L4
- Moradinezhad Dizgah, A., Keating, G. K., Karkare, K. S., Crites, A., & Choudhury, S. R. 2022a, *ApJ*, **926**, 137

- Moradinezhad Dizgah, A., Nikakhtar, F., Keating, G. K., & Castorina, E. 2022b, [JCAP](#), **02**, 026
- Nicolis, A., Rattazzi, R., & Trincherini, E. 2009, [PhRvD](#), **79**, 064036
- Padmanabhan, H. 2018, [MNRAS](#), **475**, 1477
- Padmanabhan, H. 2019, [MNRAS](#), **488**, 3014
- Poulin, V., Smith, T. L., Karwal, T., & Kamionkowski, M. 2019, [PhRvL](#), **122**, 221301
- Pritchard, J. R., & Loeb, A. 2012, [RPPH](#), **75**, 086901
- Pullen, A. R., Serra, P., Chang, T.-C., Dore, O., & Ho, S. 2018, [MNRAS](#), **478**, 1911
- Rakhi, R., & Indulekha, K. 2009, [arXiv:0910.5406](#)
- Raveri, M., Bull, P., Silvestri, A., & Pogosian, L. 2017, [PhRvD](#), **96**, 083509
- Righi, M., Hernandez-Montegudo, C., & Sunyaev, R. 2008, [A&A](#), **489**, 489
- Sailer, N., Castorina, E., Ferraro, S., & White, M. 2021, [JCAP](#), **12**, 049
- Sailer, N., Chen, S.-F., & White, M. 2022, [JCAP](#), **10**, 007
- Sakstein, J., & Jain, B. 2017, [PhRvL](#), **119**, 251303
- Sargsyan, L., Lebouiteiller, V., Weedman, D., et al. 2012, [ApJ](#), **755**, 171
- Schaan, E., & White, M. 2021a, [JCAP](#), **05**, 067
- Schaan, E., & White, M. 2021b, [JCAP](#), **05**, 068
- Schöneberg, N., Franco Abellán, G., Pérez Sánchez, A., et al. 2022, [PhR](#), **984**, 1
- Scott, B. R., Karkare, K. S., & Bird, S. 2023, [MNRAS](#), **523**, 4895
- Seljak, U. 2009, [PhRvL](#), **102**, 021302
- Silva, M. B., Santos, M. G., Cooray, A., & Gong, Y. 2015, [ApJ](#), **806**, 209
- Simon, T., Zhang, P., Poulin, V., & Smith, T. L. 2023, [PhRvD](#), **107**, 063505
- Smith, T. L., Poulin, V., & Amin, M. A. 2020, [PhRvD](#), **101**, 063523
- Speagle, J. S., Steinhardt, C. L., Capak, P. L., & Silverman, J. D. 2014, [ApJS](#), **214**, 15
- Traykova, D., Bellini, E., Ferreira, P. G., et al. 2021, [PhRvD](#), **104**, 083502
- Umiltà, C., Ballardini, M., Finelli, F., & Paoletti, D. 2015, [JCAP](#), **08**, 017
- Urena-Lopez, L. A., & Matos, T. 2000, [PhRvD](#), **62**, 081302
- Voisin, G., Cognard, I., Freire, P. C. C., et al. 2020, [A&A](#), **638**, A24
- Zumalacárregui, M., Bellini, E., Sawicki, I., Lesgourgues, J., & Ferreira, P. G. 2017, [JCAP](#), **08**, 019